





## 20 Abstract

21 Aerosol optical depth (AOD) has become a crucial metric for assessing global  
22 climate change. Although global and regional AOD trends have been studied  
23 extensively, it remains unclear what factors are driving the inter-decadal variations in  
24 regional AOD and how to quantify the relative contribution of each dominant factor.  
25 This study used a long-term (1980–2016) aerosol dataset from the Modern-Era  
26 Retrospective Analysis for Research and Applications, version 2 (MERRA-2)  
27 reanalysis, along with two satellite-based AOD datasets (MODIS/Terra and MISR)  
28 from 2001 to 2016, to investigate the long-term trends in global and regional aerosol  
29 loading. Statistical models based on emission factors and meteorological parameters  
30 were developed to identify the main factors driving the inter-decadal changes of  
31 regional AOD and to quantify their contribution. Evaluation of the MERRA-2 AOD  
32 with the combined in-situ measurements of AERONET and the China Aerosol  
33 Remote Sensing Network indicated significant spatial agreement on the global scale  
34 ( $r = 0.84$ , RMSE = 0.14, and MAE = 0.07). In general, MERRA-2 was able to  
35 quantitatively reproduce the annual and seasonal AOD trends on both regional and  
36 global scales, as observed by MODIS/Terra, albeit some differences were found when  
37 compared to MISR. Over the 37-year period in this study, significant decreasing  
38 trends were observed over Europe and the eastern United States. In contrast, eastern  
39 China and South Asia showed AOD increases, but the increasing trend of the former  
40 reversed sharply in the most recent decade. The statistical analyses suggested that the  
41 meteorological parameters explained a larger proportion of the AOD variability  
42 (20.4%–72.8%) over almost all regions of interest (ROIs) during 1980–2014 when  
43 compared with emission factors (0%–56%). Further analysis also showed that SO<sub>2</sub>  
44 was the dominant emission factor, explaining 12.7%–32.6 % of the variation in AOD  
45 over anthropogenic aerosol–dominant regions, while BC or OC was the leading factor  
46 over the biomass burning–dominant (BBD) regions, contributing 24.0%–27.7% of the  
47 variation. Additionally, wind speed was found to be the leading meteorological  
48 parameter, explaining 11.8%–30.3% of the variance over the mineral dust–dominant  
49 regions, while ambient humidity (including soil moisture and relative humidity) was  
50 the top meteorological parameter over the BBD regions, accounting for 11.7%–35.5%  
51 of the variation. The results of this study indicate that the variation in meteorological  
52 parameters is a key factor in determining the inter-decadal change in regional AOD.

53

## 54 1. Introduction

55 Atmospheric aerosols play a key role in the energy budget of the Earth's climate  
56 system through aerosol–radiation interactions (direct effect) and aerosol–cloud  
57 interactions (indirect effect). On the one hand, by absorbing and scattering solar and  
58 terrestrial radiation, aerosols generally cool the Earth's surface and heat the atmosphere,  
59 depending on the absorption level of the aerosols (McCormick and Ludwig 1967; Ding  
60 et al., 2016; Sun et al., 2018; Zheng et al., 2019). This effect is termed the aerosol direct  
61 effect. The cooling effect of aerosols may partly counteract the warming caused by the



62 increase in CO<sub>2</sub> and other greenhouse gases in the past several decades (IPCC, 2007).  
63 On the other hand, by acting as cloud condensation nuclei or ice nuclei, not only can  
64 aerosols alter the microphysical and radiative properties of clouds, as well as their  
65 lifetimes (Rosenfeld et al., 2019; Andreae 2009), but they can also change the  
66 precipitation efficiency [depending on the aerosol type (Jiang et al., 2018)], modify the  
67 characteristics of the atmospheric circulation, and affect the global hydrological cycle  
68 (Ramanathan et al., 2001; Ackerman et al., 2000; Hansen et al., 1997; Sarangi et al.,  
69 2018). This effect is termed the aerosol indirect effect. Furthermore, depending on their  
70 physical and chemical properties, as well as their composition, aerosols can affect  
71 ecosystems (Yue et al., 2017; Liu et al., 2017), atmospheric visibility (Che et al., 2007;  
72 Wang et al., 2009; Che et al., 2014), and even human health [such as through their roles  
73 in lung cancer, respiratory infection, and cardiovascular disease (Silva et al., 2013;  
74 Lelieveld et al., 2015; Cohen et al., 2017)]. Unlike the long-lived greenhouse gases (e.g.,  
75 CO<sub>2</sub>, CH<sub>4</sub> and N<sub>2</sub>O), aerosols produced via anthropogenic activity or naturally have  
76 relatively short life spans and large spatial and temporal variability. Therefore, it is  
77 essential to investigate the long-term variability and inter-decadal trends of atmospheric  
78 aerosol loadings on both regional and global scales.

79 Aerosol optical depth (AOD), representing the attenuation of sunlight induced by  
80 aerosols and serving as an important measure of aerosol loading, has become a crucial  
81 metric in assessing global climate change and the effects of aerosols on radiation,  
82 precipitation and clouds. Through the efforts of scientists in various countries over the  
83 past three decades, a series of AOD datasets with different time spans derived from  
84 continuous ground-based and satellite observations have been accumulated. These  
85 datasets have been widely employed to investigate the long-term annual and seasonal  
86 trends of AOD at global and regional scales. Although ground-based observations have  
87 limited spatial and/or temporal coverage, they can provide more detailed information on  
88 aerosol properties and long-term variations for satellite and model validation. For  
89 example, using the long-term and high-quality AOD datasets from the Aerosol Robotic  
90 Network (AERONET), Li et al. (2014) found that North America and Europe  
91 experienced a uniform decrease in AOD from 2000 to 2013. Che et al. (2015) estimated  
92 the change in AOD based on AOD data at 12 long-term ground-based sites in China  
93 from the China Aerosol Remote Sensing Network (CARSNET) and found that AOD  
94 showed a downward trend from 2006 to 2009 and an upward trend from 2009 to 2013.  
95 Compared with the spatial sparseness of ground-based observations, inferences from  
96 satellite-based sensors can provide a global perspective of AOD change, due to their  
97 continuous spatial measurements. Previous studies (Hsu et al., 2012; Pozzer et al., 2015;  
98 Mehta et al., 2016; Klingmüller et al., 2016; De Leeuw et al., 2018; Zhang and Reid  
99 2010) have investigated global and regional AOD trends by using multiple satellite  
100 observations, including the Moderate Resolution Imaging Spectroradiometer (MODIS),  
101 Multiangle Imaging Spectroradiometer (MISR), the Sea-viewing Wide Field-of-view  
102 Sensor (SeaWiFS), and others. These studies have shown increased AODs over eastern  
103 China, India, the Middle East (ME), and the Bay of Bengal, and decreased AODs over  
104 the eastern United States (EUS) and Europe.

105 In general, regional AOD changes are closely linked to the variations in natural



106 emissions driven by meteorological conditions (such as mineral dust) and local  
107 anthropogenic emissions associated with economic and population growth. For example,  
108 over anthropogenic aerosol-dominant regions, most of the primary pollutant emissions  
109 [such as black carbon (BC)] and aerosol precursors (such as SO<sub>2</sub>, NO<sub>x</sub> and NH<sub>3</sub>) in  
110 North America and Europe have declined in response to emissions control (Hammer et  
111 al., 2018). In contrast, pollutant emissions and their precursors in the rapidly developing  
112 countries (such as India and China) have increased over the past few decades,  
113 attributable to enhanced industrial activity. However, as a consequence of clean-air  
114 actions, anthropogenic emissions in China have declined significantly in recent years  
115 (Zheng et al., 2018). It has been proven that these changes in local pollutant emissions or  
116 aerosol precursors over the above regions can to a certain extent explain the regional  
117 AOD variability, as observed in long-term satellite aerosol data records (Meij et al.,  
118 2012; Itahashi et al., 2012; Feng et al., 2018). On the other hand, various studies have  
119 shown that meteorological changes play a major role in determining the inter-decadal  
120 trend of AOD over mineral dust-dominant regions, particularly in the Sahara Desert (SD)  
121 and the ME (Pozzer et al., 2015; Klingmüller et al., 2016). Based on model simulations  
122 during 2001–2010, Pozzer et al. (2015) suggested that, over biomass burning-dominant  
123 regions, the changes in both meteorology and emissions are equally important for  
124 driving AOD trends. Considering the localized changes in anthropogenic aerosol  
125 emissions and meteorological conditions in different regions, a key question is whether  
126 these factors are responsible for the regional AOD trends, or which main factors  
127 dominate the trends. Therefore, it is important to investigate the cause of regional AOD  
128 trends in terms of the variations in both anthropogenic emissions and meteorological  
129 factors for projecting the response of the earth system to future changes.

130 In this study, we used a long-term (1980–2016) aerosol dataset obtained from the  
131 Modern-Era Retrospective Analysis for Research and Applications, version 2  
132 (MERRA-2) reanalysis, along with two satellite-based datasets (MODIS/Terra and  
133 MISR) during 2001–2016, to conduct a comprehensive estimation of global and regional  
134 AOD trends over different periods. To ensure the reliability of the trend assessment, 468  
135 AERONET sites and 37 CARSNET sites with continuous observations for at least one  
136 year were used to assess the performance of the MERRA-2 AOD on a global scale.  
137 Twelve regions dominated by different aerosol types were selected to explore the  
138 relationships between local anthropogenic emissions, meteorological factors, and  
139 regional AOD. Furthermore, stepwise multiple linear regression (MLR) models were  
140 developed to estimate the regional AOD as a function of emission factors and other  
141 meteorological parameters, which allowed the influences of emissions and meteorology  
142 to be separated. Then, the Lindeman, Merenda and Gold (LMG) method was applied to  
143 the MLR models to identify the main factors driving the regional AOD variability and to  
144 quantitatively evaluate the contribution of each driving factor.

145  
146  
147  
148  
149



## 150 2. Data and methods

### 151 2.1 MERRA-2 aerosol reanalysis data

152 MERRA-2 is the latest atmospheric reanalysis version for the modern satellite era  
153 provided by the NASA Global Modeling and Assimilation Office (Gelaro et al., 2017),  
154 using the Goddard Earth Observing System, version 5 (GEOS-5), earth system model  
155 (Molod et al., 2012, 2015), which includes atmospheric circulation and composition,  
156 ocean circulation and land surface processes, and biogeochemistry. Note that, in  
157 MERRA-2, in addition to providing assimilation of traditional meteorological  
158 observations, a series of AOD observation datasets, including bias-corrected AODs  
159 retrieved from the Advanced Very High Resolution Radiometer instrument over the  
160 oceans (Heidinger et al., 2014) and MODIS (onboard both the Terra and Aqua  
161 satellites) (Levy et al., 2010; Remer et al., 2005), and non-bias-corrected AODs  
162 retrieved from MISR (Kahn et al., 2005) over bright surfaces and ground-based  
163 AERONET observations (Holben et al., 1998), were also assimilated within the  
164 GEOS-5 earth system model. An overview of the MERRA-2 modeling system and a  
165 more detailed description of aerosols in the MERRA-2 system can be found in Gelaro  
166 et al. (2017) and Buchard et al. (2017), respectively. In this study, the three-hourly  
167 instantaneous AOD datasets, at a resolution of  $0.5^\circ$  latitude by  $0.625^\circ$  longitude, were  
168 used for evaluation, while the monthly mean AOD values were used for climate  
169 analysis.

### 170 2.2 Satellite aerosol data

171 Two AOD datasets during 2001–2016 retrieved from MODIS and MISR, both  
172 onboard the Terra platform, were used in this study. The MODIS sensor onboard the  
173 Terra satellite observes the Earth at multiple wavelengths (range: 410–1450 nm; 36  
174 bands) with a 2330-km swath, which has provided near-daily global coverage since  
175 2000 (King et al., 2003; Levy et al., 2015). This study employed the combined Dark  
176 Target/Deep Blue AOD algorithm at 550 nm, with a  $1^\circ \times 1^\circ$  resolution, from the Level  
177 3 monthly global aerosol dataset for MODIS Terra, Collection 6.1. Note that  
178 MODIS/Aqua L3 was not used because it started late (June 2002). In addition,  
179 compared with MODIS/Aqua AOD monthly datasets, MODIS/Terra AOD shows  
180 similar performance worldwide (Fig. S1). Thus, with its longer observation time,  
181 MODIS/Terra was used in this study. The expected errors of the Level 2 MODIS  
182 AOD data have been estimated to be about  $\pm(0.03 + 0.05 \times \text{AOD})$  over ocean and  
183  $\pm(0.05 + 0.15 \times \text{AOD})$  over land (Levy et al., 2013).

184 Total column AOD observations from the MISR sensor onboard the Terra  
185 satellite, which provides observations of the Earth and atmosphere with nine different  
186 along-track viewing zenith angles at four different spectral bands (440–866 nm)  
187 (Diner et al., 1998), were utilized. It should be noted that, although MISR has a much  
188 narrower swath ( $\sim 360$  km) compared with MODIS, the multi-angle observation from  
189 MISR provides the capability for retrieving a more reliable AOD over bright surfaces  
190 such as desert areas (Diner et al., 1998; Kahn et al., 2010). The AOD retrieval in the



191 555-nm channel from monthly global aerosol datasets at a spatial resolution of  $0.5^\circ \times$   
192  $0.5^\circ$  were used in this study. The uncertainty of the MISR Level 2 AOD data over land  
193 and ocean has been estimated to be  $\pm 0.05$  or  $\pm(0.2 \times \text{AOD})$  (Kahn et al., 2005). Note  
194 that the wavelength of AOD (555 nm) reported by MISR is different from that of the  
195 MERRA-2 and MODIS/Terra datasets (550 nm); however, this slight wavelength  
196 difference is not expected to affect our analysis and conclusions regarding AOD  
197 annual and seasonal trends.

### 198 **2.3 Ground-based reference data: AERONET and CARSNET**

199 Owing to the accuracy of ground-based AOD observations, long-term  
200 instantaneous AOD observation records from two independent operational  
201 networks—AERONET and the CARSNET—were used to validate the three-hourly  
202 MERRA-2 AOD values. Since there are not enough long-term AERONET  
203 observations in China, it was necessary to examine the performance of the MERRA-2  
204 analyzed AOD fields using additional AOD observations from CARSNET.  
205 CARSNET is a ground-based network for monitoring aerosol optical properties that  
206 was first established by the China Meteorological Administration in 2002 (Che et al.,  
207 2009). Both AERONET and CARSNET use the same types of sunphotometers, which  
208 can observe direct solar and sky radiances at seven wavelengths (typically 340, 380,  
209 440, 500, 670, 870 and 1020 nm) within a  $1.2^\circ$  full field of view at intervals of about  
210 15 min (Holben et al., 1998; Che et al., 2009). For CARSNET, operating instruments  
211 are calibrated and standardized using CARSNET reference instruments, which in turn  
212 are regularly calibrated at Izaña, Tenerife, Spain, together with the AERONET  
213 program (Che et al., 2009; Che et al., 2018). The cloud-screened AOD [based on the  
214 work of Smirnov et al. (2000)] in CARSNET has the same accuracy as AERONET,  
215 with an estimated uncertainty of 0.01–0.02 (Eck et al., 1999; Che et al., 2009).

216 In this work, we collected ground-based AOD observations (more than one year  
217 of data) from 468 AERONET sites worldwide and 37 CARSNET sites in China. The  
218 locations of these ground-based sites are shown in Fig. 1. Detailed information about  
219 these AERONET and CARSNET sites is given in Tables S4 and S5. The combined  
220 instantaneous AOD data collected by AERONET (quality-assured and cloud-screened  
221 Level 2.0 data) during 1993–2016 and CARSNET (cloud-screened Level 2.0 data)  
222 during 2002–2014 were used. Moreover, to ensure the reliability of AOD evaluation,  
223 the AOD measurements in two adjacent channels (i.e., 440 and 675 nm) from  
224 AERONET and CARSNET were subsequently interpolated to 550 nm for MERRA-2,  
225 using a second-order polynomial fit to  $\ln(\text{AOD})$  vs.  $\ln(\text{wavelength})$  (Eck et al.,  
226 1999).

### 227 **2.4 Emissions inventory and meteorological data**

228 The anthropogenic emissions inventories used in this study were obtained from  
229 the Peking University (PKU) website (<http://inventory.pku.edu.cn/>), including total  
230 suspended particles (TSP) (Huang et al., 2014),  $\text{SO}_2$  (Su et al., 2011), BC (Wang et al.,  
231 2014), and organic carbon (OC) (Huang et al., 2015), with a spatial resolution of  $0.1^\circ$   
232  $\times 0.1^\circ$  and spanning the period 1980–2014. The emissions were calculated using a





233 bottom-up approach based on fuel consumption and an emissions factor database.  
234 Huang et al. (2015) showed that the PKU emissions inventories are broadly similar to  
235 those of EDGARv4.2 (Edgar, 2011). Monthly meteorological fields from the  
236 MERRA-2 global reanalysis were also utilized, including total surface precipitation,  
237 surface wind speed, surface relative humidity (RH), mean sea level pressure, et. These  
238 data have a spatial resolution of  $0.5^\circ \times 0.625^\circ$  and span the period 1980–2016 (Gelaro  
239 et al., 2017). For more detailed information on the selected meteorological parameters,  
240 see Table 1.

## 241 2.5 ROIs

242 In this study, 12 regions of interest (ROIs) dominated by different aerosol types  
243 were selected to study the long-term trends in regional aerosol loading and how they  
244 are related to local emission changes as well as the variation in meteorological  
245 variables. These 12 ROIs included three mineral dust–dominant regions [SD (17 °W–  
246 20 °E, 3 °N–25 °N), ME (38 °E–56 °E, 14 °N–33 °N), and Northwest China (NWC;  
247 73 °E–94 °E, 35 °N–47 °N)], three biomass burning–dominant regions [the Amazon  
248 Zone (AMZ; 46 °W–60 °W, 1 °S–22 °S), Central Africa (CF; 12 °E–33 °E, 2 °S–18 °S)  
249 and Southeast Asia (SEA; 96 °E–127 °E, 8 °S–18 °N)], and six anthropogenic aerosol–  
250 dominant regions [EUS (73 °W–94 °W, 29 °N–45 °N), western Europe (WEU; 10 °W–  
251 18 °E, 37 °N–59 °N), South Asia (SA; 72 °E–90 °E, 10 °N–30 °N), northern China (NC;  
252 108 °E–120 °E, 30 °N–40 °N), southern China (SC; 108 °E–120 °E, 20 °N–30 °N) and  
253 Northeast Asia (NEA; 125 °E–145 °E, 30 °N–41 °N)]. The geographical boundaries of  
254 these ROIs are shown in Fig. 1.

## 255 2.6 Statistical analysis

### 256 2.6.1 Comparison methods

257 AOD data from the 468 AERONET sites worldwide and the 37 CARSNET sites  
258 in China were used to evaluate the performance of the three-hourly AOD datasets  
259 from MERRA-2. To ensure the accuracy of the assessment, instantaneous  
260 ground-based AOD observations within one hour, obtained from AERONET and  
261 CARSNET, were averaged as the hourly mean AOD and compared with those from  
262 the MERRA-2 three-hourly AOD datasets.

263 The errors and quality of the MERRA-2 AOD retrievals are reported using the  
264 mean absolute error [MAE, Eq. (1)], root-mean-square error [RMSE, Eq. (2)] and the  
265 relative mean bias [RMB, Eq. (3)]. In addition, linear regression parameters were also  
266 included in this study, including the slope, the  $y$ -intercept, and correlation coefficient  
267 ( $R$ ).

$$\text{MAE} = \frac{1}{n} \sum_{i=1}^n |\text{AOD}_{(\text{MERRA-2})i} - \text{AOD}_{(\text{Ground-based})i}| \quad (1)$$

$$\text{RMSE} = \sqrt{\frac{1}{n} \sum_{i=1}^n (\text{AOD}_{(\text{MERRA-2})i} - \text{AOD}_{(\text{Ground-based})i})^2} \quad (2)$$



$$\text{RMB} = \left( \frac{\text{AOD}_{\text{MERRA-2}}}{\text{AOD}_{\text{Ground-based}}} \right) \quad (3)$$

## 268 2.6.2 Trend analysis and stepwise MLR model

269 Long-term trend analysis of the AOD from MERRA-2, MODIS/Terra and MISR  
270 was performed, on monthly time series data, using ordinary least-squares linear  
271 regression—a technique widely employed for trend analysis of aerosol data (Hsu et al.,  
272 2012; Pozzer et al., 2015; Klingmüller et al., 2016; Ma et al., 2016; Hammer et al.,  
273 2018). Prior to regression, these data were first deseasonalized by subtracting the  
274 monthly mean for different study periods for each grid cell to eliminate the large  
275 influence of the annual cycle. To better compare the results of the trend analysis, the  
276 MERRA-2 and MISR datasets at high spatial resolution ( $0.5^\circ \times 0.625^\circ$  and  $0.5^\circ \times 0.5^\circ$ ,  
277 respectively) were re-gridded to the MODIS/Terra resolution of  $1^\circ \times 1^\circ$ . Incomplete  
278 sampling from the satellite instruments may introduce biases in long-term trend  
279 analysis. Thus, to ensure the reliability of the trend analysis, each grid cell for the  
280 MISR and MODIS/Terra AODs was required to have valid data for at least 60% of the  
281 time period before regression was performed. Two-tailed Student's *t*-tests were used  
282 to assess the robustness of each trend estimate, and the criterion for statistical  
283 significance was set at the 95% confidence level.

284 Pearson's *R* was used to measure the strength of the relationship between AOD,  
285 anthropogenic emissions, and meteorological parameters. MLR models of monthly  
286 MERRA-2 AODs were built for the 12 ROIs using emission factors, meteorological  
287 parameters, and both, as predictors. Four emission factors and 32 meteorological  
288 parameters were considered in the MLR models (Table 1). For each ROI, the MLR  
289 model could be expressed as

$$y = \beta_0 + \sum_{i=1}^n \beta_i x_i + \varepsilon, \quad (4)$$

290 where *y* is the standardized monthly AOD and ( $x_1, \dots, x_n$ ) is the ensemble of  
291 standardized monthly explanatory variables. The standardized regression coefficient  
292  $\beta_i$  was determined by the least-squares method, and  $\varepsilon$  is an error term.

293 In each step of the MLR model, a variable is considered to be moved or removed  
294 from the set of explanatory variables using the stepwise regression method to obtain  
295 the best model fit. In other words, for each step the model adds a significant ( $P < 0.05$ )  
296 explanatory variable to the model, it can be removed only if it is insignificant ( $P > 0.1$ )  
297 after adding or removing another variable. A similar model has been widely used to  
298 investigate the relationship between aerosols and meteorology (e.g., Yang et al., 2016;  
299 Tai et al., 2010).

300 Although the most important explanatory variables were obtained via the above  
301 stepwise MLR model, there might be multiple collinearities among different  
302 explanatory variables. In that situation, the standardized regression coefficient as an  
303 explanation of relative importance is unstable and misleading. To eliminate the  
304 influence of multi-collinearity, the variance inflation factor (VIF) (Altland et al., 2006)





305 was used to test whether there was a multi-collinearity problem among the variables.  
306 VIF is often regarded as a measure of collinearity between each variable and another  
307 variable in the model. VIF can be calculated from the following relationship:

$$\text{VIF} = \frac{1}{1 - R_i^2}, \quad (5)$$

308 where  $R_i^2$  is the coefficient of determination of linear regression between the  $i$ th  
309 independent variable and other independent variables in the model. The present study  
310 used a VIF threshold of 10, which is widely recommended in the literature (e.g., Hair  
311 et al., 2010; Barnett et al., 2006; Field, 2005), to represent the maximum acceptability  
312 of collinearity.

313 Finally, to better quantify the relative contributions of each independent  
314 explanatory variable, which were obtained from the stepwise MLR model, to AOD  
315 variability, the LMG method (Bi 2012; Grömping 2006; Lindeman et al., 2014) was  
316 applied. This approach is one of the most advanced methods for determining the  
317 relative importance of explanatory variables in a linear model and provides a  
318 decomposition of the fraction of model-explained contributions (i.e.,  $R^2$ ) into  
319 nonnegative contributions using semi-partial  $R$  values. The LMG measure for the  $i$ th  
320 regressor  $x_i$  can be expressed as

$$\text{LMG}(x_i) = \frac{1}{p!} \sum_{r \text{ permutation}} \text{seq}R^2(\{x_i\}|r), \quad (6)$$

321 where  $r$  represents the  $r$ th permutation ( $r = 1, 2, \dots, p!$ ), and  $\text{seq}R^2(\{x_i\}|r)$  represents  
322 the sequential sum of squares for the regressor  $x_i$  in the ordering of the regressors in  
323 the  $r$ th permutation.

324 For a detailed introduction to and description of the calculation process of the  
325 LMG measure, refer to Grömping (2006). For all variables (including the AODs from  
326 MERRA-2, MISR and MODIS/Terra, the meteorological variables from MERRA-2,  
327 and the emission estimates from PKU), the regional mean was calculated by  
328 averaging valid variable values over all grids within the twelve ROIs. For the seasonal  
329 analysis, the four seasons were considered as follows: spring (March–April–May),  
330 summer (June–July–August), autumn (September–October–November), and winter  
331 (December–January–February).



### 332 **3 Results and discussion**

#### 333 **3.1 Assessing the performance of the MERRA-2 AOD datasets**

##### 334 **on the global scale**

335 Although the official documentation points out that a large number of AOD  
336 observations have been assimilated into the system (Buchard et al., 2017), the global  
337 performance of MERRA-2 AOD is still unknown. Using all of the collected  
338 AERONET and CARSNET observations, the overall performance of the MERRA-2  
339 AOD on a global scale was validated first. The results showed significant spatial  
340 agreement between MERRA-2 and ground-based AOD on the global scale, with an  
341 acceptable bias ( $r = 0.84$ , RMSE = 0.14, and MAE = 0.07) (Fig. 2). Moreover, Fig. 3  
342 shows site-to-site comparisons of the three-hourly MERRA-2 AOD at 550 nm and the  
343 collocated AEROENT and CARSNET AOD observations, and a statistical summary  
344 of the comparison and the location information for each site are given in Tables S4  
345 and S5. Globally, the MERRA-2 AOD datasets exhibited high  $R$  values against  
346 ground-based observations: over 83.2%, 58.0% and 26.1% of sites had an  $R$  greater  
347 than 0.6, 0.7 and 0.8, respectively; 80.4% and 47.1% of sites had an MAE greater than  
348 0.1 and 0.05, respectively; and more than 65.3% and 85.1% of sites had an RMSE less  
349 than 0.1 and 0.2, respectively. These results indicated that, although MERRA-2 does  
350 not perform well in some individual regions, it does not affect the global accuracy of  
351 MERRA-2 as the latest global aerosol reanalysis dataset, especially in comparison  
352 with other satellite datasets. In addition, the obvious regional differences in the global  
353 performance of MERRA-2 AOD should not be overlooked. According to Fig. 3c1, the  
354 RMB was greater than 1 in the United States, southern South America and Australia,  
355 which indicates that MERRA-2 overestimates the AOD in these regions. In contrast,  
356 there clear underestimation was found in other regions, such as the Amazon Basin,  
357 Europe, SA, and SEA. This apparent underestimation (about 29%) in NC was further  
358 confirmed using additional ground-based AOD observations from CARSNET  
359 (reported in the following section). Notably, this underestimation seems to be  
360 systematic, as negative RMB was found in most parts of the Northern Hemisphere,  
361 except the United States. Such systematic underestimation over these regions is likely  
362 due to the lack of nitrate aerosols in the GOCART model (Buchard et al., 2017).  
363 Furthermore, the underestimation seems to be more prominent in high  
364 nitrate-emissions areas such as NC and SA.

365 To ensure the accuracy of inter-annual variations of AODs over different ROIs (as  
366 defined in Fig. 1), the regional performance of MERRA-2 AOD was evaluated by  
367 integrating all sites within each ROI (Figs. S2 and S3). Regionally,  $R$  ranged from 0.7  
368 to 0.95 among the 12 ROIs, with the highest  $R$  (0.95) occurring in the ME and the  
369 lowest (0.7) in the EUS. Similar to the site-to-site RMB distribution, the RMB  
370 presented a systematic overestimation in the EUS of around 11%. In contrast, the  
371 RMB showed significant systematic underestimation in NC, SA, CF and SEA, with  
372 the degree of underestimation being 29%, 13%, 25% and 16%, respectively.



373 Significant differences in these regions were also supported by large MAEs of 0.25,  
374 0.11, 0.08 and 0.12, respectively.

375 The MERRA-2 AOD datasets performed better over SA than over NC, which is  
376 one of the most polluted areas in the world, in terms of a smaller MAE (0.11) and  
377 RMSE (0.18) (Fig. S2f). The better performance over SA is likely due to more AOD  
378 observations having been assimilated in MERRA-2 compared to over NC (Buchard et  
379 al., 2017). For NEA, SC and WEU, MERRA-2 AOD generally compared well to  
380 AERONET AOD, with the MAE being less than 0.1 and RMB greater than 0.93. For  
381 the SD, results were relatively poor in that the MAE was greater than 0.1 and the  
382 RMSE greater than 0.2. Besides, although MERRA-2 performed well in NWC when  
383 only one AERONET site was used, after using additional CARSNET ground-based  
384 observations it was found that the MERRA-2 AOD performance in NWC needs to be  
385 improved (Fig. S3c). Notably, MERRA-2 was found to produce lower AOD than  
386 AERONET, and the bias between them was more obvious for high AERONET AODs.  
387 For instance, the MERRA-2 AODs over most polluted areas (such as the  
388 anthropogenic aerosol-dominant regions of NC and SA and the biomass burning-  
389 dominant regions of SEA and South America) were almost always lower than those of  
390 AERONET when the AERONET AOD was greater than 1.5. This indicated that  
391 MERRA-2 does not capture all high-AOD events well (such as serious haze events  
392 over NC and SA, and frequent biomass burning events over SEA), due to the  
393 following three reasons: (1) a relatively low quantity of ground-based-observed  
394 aerosol data can be used for assimilation; (2) the MERRA-2 system model lacks an  
395 adequate source of anthropogenic emissions with high temporal resolution; and (3) a  
396 lack of nitrate aerosols in the GOCART model (Chin et al., 2002; Colarco et al., 2010;  
397 Buchard et al., 2017).

398 To confirm whether MERRA-2 systematically underestimates the AOD over NC,  
399 additional AOD observations from 12 CARSNET sites within NC were used for  
400 comparison, and the corresponding statistical results for the site-by-site comparison  
401 are given in Table S5. Compared with the results from using three AERONET sites as  
402 a comparison, the results comparing CARSNET and MERRA-2 AOD showed a  
403 similar pattern—that is, the underestimation of MERRA-2 AOD over NC is universal.  
404 MERRA-2 underestimated the AOD at almost all CARSNET sites (Fig. 3c2 and Table  
405 S5), with an overall MAE of 0.23, RMSE of 0.33, and underestimation of ~29% (Fig.  
406 S3a). Similar results based on CARSNET observations in China have also been  
407 reported in the literature (Song et al., 2018; Qin et al., 2018). Specifically, there was  
408 higher agreement over SC compared with NC (Fig. S3b), mainly because nitrate  
409 aerosols in China are mainly concentrated in industrially intensive areas such as  
410 Henan, Shandong, Hebei, and the Sichuan Basin (Zhang et al., 2012). The lack of a  
411 nitrate module in the GOCART model will cause further AOD uncertainty in these  
412 above areas, which is the main reason behind the relatively low performance of  
413 MERRA-2 AOD in these areas.

414 The purpose of this work was to study the inter-annual or inter-decadal variations  
415 of AOD in different regions. Therefore, taking MODIS/Terra and MISR AOD as a  
416 reference, the accuracy of MERRA-2 annual-mean AOD was evaluated at global and



417 regional scales (Figs. S4 and S5). Globally, the overall spatial correlations between  
418 the MERRA-2 AOD and MODIS/Terra and MISR AOD datasets was found to be  
419 quite acceptable, with no apparent disagreements in the annual AOD variations during  
420 2001–2016 (Fig. S5). Besides, although an offset was found between MERRA-2,  
421 MODIS/Terra and MISR in terms of absolute values of AOD in some ROIs, the  
422 short-term tendency during the overlapping period was similar among the three  
423 datasets (Fig. S4). Because the aerosol retrieval algorithm based on satellite  
424 observation does not work well under cloudy conditions or for bright surfaces, there  
425 are always numerous missing values in satellite-retrieved AOD datasets. In contrast,  
426 not only is the accuracy of the MERRA-2 AOD dataset comparable with satellite  
427 observations (Fig. S4), it also provides a complete AOD record from 1980 to the  
428 present day. These reasons give confidence that the MERRA-2 aerosol dataset is  
429 suitable for analysis of the variations in AOD. Thus, the AOD values from  
430 MERRA-2's aerosol analysis fields, in combination with the AOD datasets derived  
431 from two satellite sensors, were used to comprehensively analyze the spatiotemporal  
432 variability of aerosols at global and regional scales.

### 433 **3.2 Global AOD distribution and inter-annual evolution of** 434 **regional AOD**

435 Figure S6 shows the global annual- and seasonal-mean AOD distribution  
436 calculated from the MERRA-2 AOD products during 1980–2016. Furthermore, the  
437 distributional characteristics of the global annual-mean AOD from MERRA-2,  
438 MODIS and MISR during the same period (2001–2016) are also compared in the  
439 figure. The comparison shows that, although MISR underestimated the AOD (e.g., in  
440 SA and eastern China), as expected because of insufficient sampling (Mehta et al.,  
441 2016; Kahn et al., 2009), the three AOD products were generally closely consistent on  
442 the global scale (also see Fig. S5). Generally, high AOD loading was mainly observed  
443 in areas of high anthropogenic and industrial emissions, such as in eastern China and  
444 India, and major source areas of natural mineral dust—particularly the Saharan,  
445 Arabian and Taklimakan deserts.

446 Due to the seasonal variation of the atmospheric circulation driven by solar  
447 radiation and the intensity of human activities in different regions, the global  
448 distribution of AOD also shows obvious seasonal differences, with global aerosol  
449 loading reaching its maximum in spring and summer. On the one hand, this can  
450 mainly be attributed to the enhanced circulation in spring and summer, which  
451 increases the likelihood of natural mineral dust from several major dust sources in the  
452 Northern Hemisphere (i.e., the Sahara and Sahel, the Arabian Peninsula, Central Asia,  
453 and the Taklimakan and Gobi deserts) being brought into the atmosphere; plus, along  
454 the westerly belt, airflow dust can be transmitted to surrounding sea areas (such as the  
455 strip of the northern tropical Atlantic stretching between West Africa and the  
456 Caribbean, the Caribbean, the Arabian Sea, and the Bay of Bengal) and more remote  
457 areas (such as South America, the Indo-Gangetic Plain, and the eastern coastal areas  
458 of China, Korea, and Japan). On the other hand, higher temperatures and damp air in



459 summer can create favorable conditions for the hygroscopic growth and secondary  
460 formation of aerosols (Minguillón et al., 2015; Zhao et al., 2018), which raises the  
461 AOD in some areas, such as NC and northern India, dominated by anthropogenic  
462 aerosol emissions in summer. Moreover, frequent local biomass-burning aerosol  
463 emissions in central Africa during summer is the main cause of high AOD in the  
464 region (Tummon et al., 2010).

465 In contrast, global aerosol loading is relatively low in autumn and winter. The  
466 atmosphere in autumn and winter is generally more stable and vertical mixing is  
467 weaker, and thus it is difficult for more aerosols—particularly natural mineral  
468 dust—to be brought into the atmosphere, which leads to lower AOD in autumn and  
469 winter. Nevertheless, the AOD in autumn in South America, SEA, SC and CF is  
470 clearly high, which is mainly attributable to the emission of large amounts of fine  
471 aerosol particles (i.e., BC and OC) from frequent biomass burning in these regions  
472 (Thornhill et al., 2018; Ikemori et al., 2018; Chen et al., 2017). Notably, fine  
473 particulate matter composed of sulfate–nitrate–ammonium aerosols, which is  
474 produced by high-intensity anthropogenic activities in autumn and winter, is still the  
475 main contributor to high AOD in eastern China and India (Gao et al., 2018; David et  
476 al., 2018).

477 To better characterize the temporal evolution of regional AOD, the monthly mean  
478 AODs over the 12 ROIs from 1980 to 2016 were calculated. As illustrated in Fig. 4,  
479 the monthly regional AOD had large seasonal variability, in addition to varying  
480 degrees of fluctuation in different periods. In areas dominated by smoke aerosols from  
481 biomass burning (i.e., AMZ, CF and SEA), biomass-burning events tend to occur in  
482 the warm season (May to October), leading to a more prominent monthly AOD at this  
483 time of the year compared with the cold season (November to April). It is noteworthy  
484 that MERRA-2 also captured several well-known forest-fire events, such as those in  
485 Indonesia in 1983 and 1997, which have been proven to be mainly related to climatic  
486 drying caused by El Niño and large-scale deforestation (Page et al., 2002; Goldammer  
487 2007). In the CF region, the monthly mean maximum AOD experienced a  
488 transformation process—that is, the monthly maximum AOD often occurred in June  
489 and July before 2000, whereas after 2000 it occurred more frequently in August and  
490 September. In the AMZ and SEA regions, September and October seems to be the two  
491 most frequent months for the occurrence of high AOD values, but the magnitude of  
492 AOD values has decreased in recent years.

493 In areas dominated by natural mineral dust aerosol (i.e., the SD, ME and NWC),  
494 the monthly maximum AOD mainly occurred in March–August. Before 2000, there  
495 were many anomalies of the AOD monthly maximum, which also implied frequent  
496 sandstorms. In contrast, the frequency of monthly AOD anomalies decreased after  
497 2000, which may be attributable to the reduced surface wind speed and increased  
498 vegetation cover (Kim et al., 2017; Wang et al., 2018; An et al., 2018). Compared  
499 with the areas dominated by smoke and dust aerosols, the seasonal differences of  
500 AOD in the areas dominated by anthropogenic aerosol emissions appear to be smaller,  
501 but their temporal evolution is more pronounced. In NEA, the monthly maximum  
502 AOD often occurred in March–June, possibly related to the long-distance



503 transportation of sand and dust in the China–Mongolia deserts (Taklimakan and Gobi).  
504 However, as the frequency of sandstorms has decreased in the past 10 years (An et al.,  
505 2018), the monthly maximum AOD has also shown a downward trend. In NC and SA,  
506 the monthly AOD has gradually expanded outward since 1980, indicating that AOD  
507 has experienced a gradual increase. Monthly AOD had large seasonal variability in  
508 the SC region, reaching its maximum in February–April. The increased aerosol  
509 emissions from biomass burning in spring seem to be one of the main reasons for high  
510 AOD in the SC region (Chen et al., 2017). For the EUS and WEU regions, the  
511 characteristics of the monthly variation in AOD were similar—that is, large values of  
512 AOD occurred in summer. With time, the monthly AOD showed a tendency to  
513 gradually shrink inwards, suggesting AOD has experienced a significant decline over  
514 the past few decades in the EUS and WEU. The main drivers of the inter-annual  
515 variability of AOD over each ROI are discussed in detail in sections 3.5 and 3.6.

### 516 3.3 Global AOD trend maps

517 Annual and seasonal linear trends of the MERRA-2 AOD anomaly were  
518 separately calculated for each  $1^\circ \times 1^\circ$  grid cell for the whole of 1980–2016 period  
519 (period 1) and for the first 18 years (1980–1997, period 2) and last 19 years (1998–  
520 2016, period 3). Figure 5 shows the spatial distribution of these trends on the global  
521 scale. Throughout period 1, the regions where annual AOD showed a significant  
522 upward trend ( $p < 0.05$ ) were mainly located in eastern China, SA, the ME, northern  
523 South America, and the southern coastal areas of Africa, whereas some significant  
524 downward trends were observed in the whole of Europe and the EUS. However,  
525 compared with the annual trends, the seasonal AOD trends had obvious regional  
526 differences in terms of their spatial distribution. For instance, a strong positive trend  
527 throughout East Asia, including Korea and Japan, was found in spring. In summer,  
528 there was a significant upward and downward AOD trend in north-central Russia and  
529 the Amazon basin, respectively. In contrast, winter AOD had a significant downward  
530 trend in the area north of  $40^\circ\text{N}$ .

531 In the two different historical periods (i.e., period 2 and 3), these trends seem to  
532 have experienced a remarkable shift. During period 2, the annual AOD had a  
533 significant upward trend throughout the Southern Hemisphere, and similar upward  
534 trends also existed in eastern and northwestern China. This upward trend in the  
535 Southern Hemisphere, which was most likely associated with two giant volcano  
536 eruption events in the early 1980s [El Chichón (Hofmann and Rosen 1983)] and early  
537 1990s [Pinatubo volcanoes (Stenchikov et al., 1998; Bluth et al., 1992; Kirchner et al.,  
538 1999)], is also reflected in the regional annual mean AOD time series shown in Fig.  
539 S4. The eruptions led to a strong increase in volcanic ash and  $\text{SO}_2$  emissions,  
540 consequently increasing AODs from place to place via airflow transport, which was  
541 captured accurately by MERRA-2. Meanwhile, AOD had a significant downward  
542 trend throughout Europe and the EUS, which appears to be related to the reduction of  
543 TSP and  $\text{SO}_2$  emissions (see section 3.5). Seasonally, a significant upward trend  
544 seems to be prevalent in all seasons in the Southern Hemisphere. Compared with  
545 other seasons, the decline of AOD was more obvious in Europe and America. In





546 winter, except for the positive trend that still existed in the marine area of the  
547 Southern Hemisphere, the fluctuations in other regions were smaller and relatively  
548 stable.

549 During period 3, AOD began to show a significant upward trend in most regions,  
550 especially in SA, SEA, the ME, central Russia, the western United States, and  
551 northern South America, whilst still maintaining an upward trend in eastern China  
552 with greater intensity. These upward trends over SA, the ME and eastern China are in  
553 good agreement with the results of Hsu et al., (2012), who used SeaWiFS AOD  
554 records from 1997 to 2010. It is worth noting that the trends for the whole of Europe  
555 shifted from significantly positive to statistically insignificant, while the region that  
556 had shown a significant downward trend before 1997 in the EUS was also shrinking.  
557 Furthermore, the region showing a positive trend, prevailing in the Southern  
558 Hemisphere, shrunk dramatically. Similarly, the spatial distribution of the trend also  
559 had significant differences in different seasons of this period. In spring and winter,  
560 only significant upward trends could be observed on a global scale, mainly in eastern  
561 China, SA, the ME and South America. Conversely, significant downward trends  
562 were apparent in the EUS, Northwest Africa and central South America in summer.  
563 Additionally, it was also found that the region with a significant downward trend in  
564 Africa shifted from the northwest in summer to the southwest in autumn.

565 Ensuring the accuracy of AOD trends calculated by MERRA-2 is critical for  
566 quantifying the contribution of local emissions and meteorological factors to the  
567 inter-decadal variation of AOD in different regions. For comparison, the resulting  
568 annual and seasonal trends of the MERRA-2, MODIS/Terra, and MISR AOD  
569 anomaly over the whole globe were derived, using the same method, between 2001  
570 and 2016; the results are shown in Fig. 6. This comparison shows that the AOD trends  
571 during 2001–2016 calculated by MERRA-2 in most regions of the world agreed well  
572 with the results of MODIS and MISR, on both annual and seasonal timescales.  
573 Although MERRA-2 assimilates MODIS and MISR at the same time, the relatively  
574 small difference between MERRA-2 and MISR may be mainly due to the insufficient  
575 sample size of MISR (MODIS produces three to four times more data than MISR)  
576 (De Meij et al., 2012).

577 For the annual trend, the significant upward trend observed by MODIS/Terra and  
578 MISR in SA and the ME and the significant downward trend observed in the EUS,  
579 WEU and central South America were consistent with the results of the MERRA-2  
580 trend. Similar trends were reported in a previous study based upon 14 years (2001–  
581 2014) of observational records (Mehta et al., 2016). Similarly, upward trends also  
582 existed in spring, autumn and winter, while downward trends were also apparent in  
583 spring, summer and autumn. It should be noted that the trend signals calculated from  
584 MERRA-2 and MODIS/Terra were opposite in SC. The difference in sign associated  
585 with trends during 2001–2016 could mainly be due to the larger deviation between  
586 MERRA-2 and MODIS/Terra between 2001 and 2004 (Fig. S4c). The large deviation  
587 directly led to a reversal of trend throughout the period 2001–2016. This deviation  
588 may be related to the use of different versions of MODIS data: in the MERRA-2 AOD  
589 observing system, MERRA-2 assimilated the bias-corrected AOD derived from



590 MODIS radiances, Collection 5 (Buchard et al., 2017), and the MODIS data used in  
591 this study was the latest collection (Collection 6.1). Different versions mean  
592 differences in algorithms (Fan et al., 2017), which may affect the statistical error.

### 593 3.4 Regional AOD trends

594 To examine the spatial and temporal changes in more detail, the annual trend over  
595 the globe and in the 12 ROIs, derived based upon MERRA-2 during periods 1, 2 and  
596 3, were calculated. In addition, for comparison purposes, the regional trends in AODs  
597 from MERRA-2, MODIS and MISR during 2001–2016 were also estimated. The  
598 comparisons of the magnitudes of global annual trends with these regional trends are  
599 summarized in Fig. 7 and Table S1. In general, the annual trends derived from  
600 different datasets were small on the global scale. As indicated by the results in Fig. 7  
601 and Table S1, the trend values were  $-0.00068 \text{ yr}^{-1}$  for the globe during period 1, with  
602 statistical significance at the 95% confidence level. In contrast, no statistically  
603 significant trend was detected at the global scale for period 2 ( $0.00050 \text{ yr}^{-1}$ ) or 3  
604 ( $0.00038 \text{ yr}^{-1}$ ). Analyzing the global AOD trends during 2001–2016 from MERRA-2  
605 and the two satellite datasets, it was found that the MERRA-2 trends were negligible,  
606 whereas significant positive (negative) trends were found for MODIS (MISR).

607 However, the trends could be considerable on regional scales. For example, over  
608 the anthropogenic aerosol–dominant regions for periods 1, 2 and 3, strong positive  
609 trends were apparent over NEA, NC, SC and SA, while strong and statistically  
610 significant negative trends were found over WEU and EUS. For biomass-burning  
611 regions (SEA, CF and AMZ, but not CF, which had a negligible and insignificant  
612 trend), there was a positive trend during periods 1, 2 and 3. For the mineral dust–  
613 dominant regions, although there seemed to be an upward trend over the ME, the  
614 estimated trends were not statistically significant for other areas, such as NWC and  
615 the SD. During 2001–2016, the estimated MERRA-2 AOD trend in most ROIs (i.e.,  
616 NEA, SA, ME, WEU, EUS, and AMZ) was comparable to and had the same sign as  
617 the trend from both the MODIS and MISR sensors. However, it was opposite in sign  
618 to the MISR data over NC, NWC and the SD, and to the MODIS data over SC, SEA  
619 and CF during overlapping years.

620 In addition to the annual trend, the seasonal trend of AOD for different datasets in  
621 different ROIs and different historical periods was also studied (Fig. S7 and Table S1).  
622 Globally, negative trends were observed throughout the four seasons during period 1,  
623 especially during summer, autumn and winter ( $-0.00078$ ,  $-0.00092$  and  $-0.00097 \text{ yr}^{-1}$ ,  
624 respectively; statistically significant at the 95% confidence level). On the contrary,  
625 there was a negative trend in period 2, although it was not significant. In the  
626 subsequent period, period 3, the trend values shifted from negative to positive. The  
627 positive trend was more significant in spring and autumn ( $0.00053$  and  $0.00070 \text{ yr}^{-1}$ ).  
628 Regionally, strong positive trends were apparent over both NC and SC throughout the  
629 four seasons during periods 1, 2 and 3. Strong upward trends were also found over SA.  
630 These upward trends were most likely associated with an increase in urban/industrial  
631 pollution in China and India. Meanwhile, some similar but relatively moderate  
632 upward trends also existed over NEA in spring. In contrast, strong negative trends



633 were observed over the WEU and EUS regions, especially during spring, summer and  
634 autumn. The negative trends over WEU and the EUS may partly have been due to a  
635 decrease in polluting aerosols associated with emission control measures. A  
636 statistically significant upward trend was also found over the SD, NWC and the ME  
637 in spring during periods 1, 2 and 3 ( $0.00252$ ,  $0.00300$  and  $0.00463 \text{ yr}^{-1}$ ), respectively.  
638 In contrast to the strong downward trends over AMZ in summer during periods 1, 2  
639 and 3, there appeared to be upward trends in spring over AMZ and in winter over CF  
640 and AMZ. When compared with the regional trends during 2001–2016 calculated by  
641 the two satellite datasets, we found that the seasonal trends of MERRA-2 were highly  
642 consistent with the satellite results in almost all regions, especially in spring and  
643 autumn. It is worth noting that the trend differences among the three different datasets  
644 in all four seasons still existed in NC and SC, and the differences had different  
645 seasonal characteristics. For example, over NC, the most significant difference  
646 occurred in spring and summer, whereas it occurred in summer and winter over SC.

647 Since the sign of a trend value often varies with the span of the calculation period,  
648 it was necessary to evaluate the sliding trend of different periods to help examine the  
649 time node of the changes more precisely. Therefore, sliding trend analyses were used  
650 to present a more comprehensive analysis of annual trends over the 12 ROIs during  
651 different historical periods (Fig. 8). These trends were calculated for all periods  
652 starting each year from 1980 to 2007 and ending in 2016 with increments of at least  
653 10 years. As shown in Fig. 8, in the EUS and WEU, the AOD experienced a large  
654 decline up until the 1981–1990 period, and then the trend reversed moderately from  
655 1984 to 1986, declined sharply from 1989 after a short increase from 1996 to 1999,  
656 and then sustained a moderate downward trend in the last 17 years. A similar pattern  
657 was found for NWC, SD and AMZ, although there was a stronger upward trend and  
658 relatively weaker downward trend in the corresponding period. In SC and NC, the  
659 AOD experienced a slight increase in the 1980s and a short-term decline around the  
660 1990s, and then showed its largest positive trend since 1995 before reversing sharply  
661 in the last 10 years. A similar evolution also existed in NEA and the ME, although the  
662 intensities of the trends were relatively weak. In addition to the negligible downward  
663 trend in the 1980s and 1990s, SA showed overall positive trends throughout the period.  
664 Furthermore, in CF, a moderate increasing trend was detected from 1983 to 1985; then  
665 in 1990, and the trends became relatively stable but unexpectedly showed sharp  
666 increases after 1993, followed by a significant decline in the 2000s and reversal in the  
667 last 10 years. The trends for SEA were much smaller and relatively stable. Also, note  
668 that around 1985 and 1990 two distinct opposite trend signs were found in all regions.  
669 These two unexpected trends indicated that large volcanic eruptions not only greatly  
670 affect short-term changes in local aerosols, but also impose different degrees of  
671 disturbance in long-term trends of aerosols in different regions of the world.

672 Furthermore, considering that aerosol concentration and composition usually  
673 have strong seasonal cycles, the trends for each season were also calculated separately  
674 and compared with the MODIS and MISR trends in the period of overlap (2001–  
675 2016). Note that Fig. 9 only shows the evolution of seasonal and annual trends for  
676 every 10-year period starting from 1980 to 2007 for MERRA-2, and from 2001 to



677 2007 for MODIS and MISR; refer to Figs. S8–11 for a fuller presentation of the  
678 regional seasonal trend. For all regions, the trends for all seasons, except autumn in  
679 SEA, CF and AMZ and spring in the SD, were in phase with the annual trend (also  
680 see Fig. S12). In general, autumn trends over SEA, CF and AMZ were larger and  
681 often out of phase, possibly attributable to the sudden increase in aerosol  
682 concentration caused by biomass-burning events. Similarly, the spring trend over the  
683 SD was also larger and more asynchronous than in other seasons. This phenomenon  
684 can mainly be attributed to active spring dust events. In addition, compared with the  
685 annual and seasonal regional trends during 2001–2016 (Fig. 7 and Fig. S7), the  
686 decadal trends of MERRA-2 agreed better with the trend results from MODIS and  
687 MISR. This implies that the trends can change relatively quickly with time.  
688 Supporting evidence was also found from the strongest trends on both annual and  
689 seasonal scales being mostly concentrated in the lower y-axis values (Fig. 9 and Figs.  
690 S8–11). These results also highlight the importance of evaluating temporal shifts or  
691 decadal AOD trends.

### 692 **3.5 Response of inter-decadal variation in regional AOD to local** 693 **emissions and meteorological parameters**

694 Previous studies have shown that the inter-annual variations in regional AOD are  
695 mainly controlled by changes in emissions and meteorological factors (De Meij et al.,  
696 2012; Pozzer et al., 2015; Itahashi et al., 2012; Zhao et al., 2017; Chin et al., 2014).  
697 First, the trends of the four emission factors (i.e., TSP, SO<sub>2</sub>, BC, and OC) and their  
698 correlations with AOD were calculated for the whole study period (1980–2014), as  
699 well as for two individual periods (i.e., 1980–1997 and 1998–2014). Note that the  
700 PKU global emissions inventories were only available for 1980–2014, which limited  
701 our research to a relatively short period. Figures 10 and S13 show the linear trends in  
702 emissions and their relationships with MERRA-2 AOD during 1980–2014,  
703 respectively. The decreasing AOD trends over Europe and the EUS (see Fig. 5)  
704 coincided with substantial reductions in the emissions of primary anthropogenic  
705 aerosols (TSP and BC) and precursor gases (SO<sub>2</sub>), corresponding to pollution controls  
706 (Hammer et al., 2018; De Meij et al., 2012). This was also supported by significant  
707 positive correlation between AOD and emissions in most regions of Europe and the  
708 EUS (Fig. S13).

709 Positive trends in TSP and SO<sub>2</sub> were present over India and eastern China, which  
710 explained the significant upward trend of AOD in these two regions. In addition,  
711 eastern China and India experienced a shift in the emissions trend during the two  
712 periods (Figs. S14 and 16). In 1980–1997, a significant upward trend existed in both  
713 regions. In contrast, in 1998–2014, India at least maintained this upward trend for all  
714 four emission factors, with it sometimes being even stronger, while the positive trends  
715 in emissions of TSP and SO<sub>2</sub> over eastern China were interspersed with negative  
716 trends. More importantly, the trend of BC and OC in eastern China reversed  
717 completely. The shift in these emission trends in eastern China can mainly be  
718 attributed to the implementation of multiple emission reduction policies (Zheng et al.,



719 2018). The reductions in emissions were at least partly responsible for the decreasing  
720 trend of AOD in the NC and SC regions in the last 10 years (see Fig. 8). The trends in  
721 primary BC emissions followed a similar pattern as the trends in OC emissions,  
722 except there were positive trends over northeastern China and the positive (negative)  
723 trends over CF, AMZ and SEA (WEU and SC) were lower in magnitude, reflecting  
724 regional changes in fire activity. There were positive AOD trends in areas dominated  
725 by biomass burning (especially in CF and SEA), in response to increased BC and OC  
726 emissions. Because human activities are scarce in desert areas, there was no direct  
727 relationship between AOD and emissions, as expected. Therefore, this highlights the  
728 importance of studying how natural factors (here, this refers to meteorological  
729 parameters) control the inter-annual variation of AOD in different desert areas.  
730 Furthermore, it is worth noting that in the two short periods (especially 1998–2014),  
731 these regions with significant positive correlation shrunk and were no longer  
732 significant (Figs. S15 and 17), suggesting other factors such as meteorological  
733 parameters might be driving the inter-annual trend of regional AOD.

734 To investigate the roles of meteorological parameters in the decadal variation of  
735 AOD, Pearson's  $R$  values between AOD and meteorological parameters (a total of 32;  
736 see Table 1) and over the 12 ROIs for the three periods (i.e., 1980–2014, 1980–1997  
737 and 1998–2014) were calculated. Some of these meteorological variables, such as  
738 surface precipitation, surface wind speed, wind velocity, RH, and surface wetness,  
739 have been shown before to be correlated with regional AOD (Klingmüller et al., 2016;  
740 Pozzer et al., 2015; Chin et al., 2014; He et al., 2016). Correlation analysis showed  
741 similar correlation patterns between AOD and meteorological parameters for the three  
742 different periods over all ROIs. During the period 1998–2014, the correlation was  
743 generally stronger than in the other two periods (see Fig. S18), suggesting  
744 meteorological factors may have played a more important role in this period. In  
745 addition, these correlations seemed to be similar in regions dominated by the same  
746 aerosol type. For example, in the mineral dust-dominated regions (i.e., NWC, ME and  
747 the SD), AOD had a significant positive (negative) correlation with near-surface wind  
748 speed (soil moisture), suggesting that surface wind speed and soil moisture may be the  
749 main factors controlling the dust cycle, which is consistent with previous studies in  
750 the ME (Klingmüller et al., 2016). In the biomass burning-dominated regions (i.e.,  
751 SEA, CF and AMZ), AOD had a significant negative correlation with  
752 humidity-related meteorological parameters (such as surface precipitation, RH, and  
753 soil moisture), implying that ambient humidity (including the atmosphere and soil)  
754 may be a direct correlation factor in controlling the frequency of biomass-burning  
755 events. In contrast, in the regions dominated by anthropogenic aerosols, the  
756 correlation was regionally dependent, and their signs differed from place to place.

757 Correlation analysis cannot directly identify the main factors affecting the  
758 inter-decadal change of AOD in different regions. Here, MLR models were used to  
759 diagnose the influences of local anthropogenic emissions and other meteorological  
760 parameters on the inter-decadal variation of AOD over the 12 ROIs. Figure 11 shows  
761 the time series of monthly mean MERRA-2 and MLR model-predicted normalized  
762 AOD anomalies, which used the emission factors, meteorological parameters, and





763 both, as input predictors, respectively, over the 12 ROIs for the whole study period  
764 (1980–2014). Similar comparisons for the two individual periods (i.e., 1980–1997 and  
765 1998–2014) are also presented in Figs. 19 and 20, respectively. Table S2 summarizes  
766 the predictors included in the MLR models and their performance for the three  
767 different periods over each ROI. The MLR models with both emissions and  
768 meteorological parameters as predictors generally reproduced the AOD values in most  
769 regions during 1980–2014, except for high AOD values (Fig.11), which is discussed  
770 below. For all the ROIs, the MLR models explained most of the MERRA-2 AOD  
771 variability ( $R^2 = 0.42$ – $0.76$ ). However, when meteorology and emissions alone were  
772 used as predictors, there were considerable differences in different ROIs. When  
773 emission factors alone were used as the predictor, it could account for more than 35%  
774 of the AOD variability in regions dominated by anthropogenic aerosols and biomass  
775 burning [except NEA (14%)], with the largest explanation occurring in NC (58%). In  
776 contrast, in the mineral dust-dominated regions (the SD and ME), emission factors  
777 contributed little ( $< 0.05\%$ ) to the inter-annual variation in AOD (Figs. 11g and i).  
778 Moreover, emission factors contributed 37% of the AOD variability in NWC, which is  
779 mainly because of the strong anthropogenic emission sources in northern Xinjiang  
780 (mainly encompassing Urumqi, Korla, Kashgar, etc.). However, compared with  
781 meteorological factors, emissions were not the main factors driving the inter-annual  
782 change of AOD (Fig. 11e).

783 On the other hand, when meteorological factors were used as predictors in the  
784 MLR models, it was surprising that they explained a larger proportion of the AOD  
785 changes in all ROIs, except NC and SEA, where emission factors accounted for  
786 slightly lower AOD changes of 42% and 33%, respectively. Further analysis indicated  
787 that this difference in contribution between emissions and meteorology seemed to be  
788 greater for the two shorter periods of 1980–1997 and 1998–2017 (see Figs. S19 and  
789 20). Besides, it should also be noted that the total explained variances of the MLR  
790 model for 1980–1997 were generally lower than those of the MLR model for 1998–  
791 2014, in all ROIs. The difference can be explained by two reasons: (1) a greater  
792 number of high AOD anomaly values occurred during the period 1980–1997 (Figs. 11  
793 and S19), especially in relation to the two volcanic eruption events in the 1980s and  
794 1990s, which directly reduced the total explained variances of the MLR model,  
795 because the model only considers the inter-decadal variations of local emissions and  
796 meteorological factors, and the large-scale transport of pollutants is not considered;  
797 and (2) meteorology and emissions were confirmed to explain more AOD changes  
798 during the period 1998–2014.

### 799 **3.6 Relative contributions of local emissions and meteorological** 800 **parameters to inter-decadal variations of regional AOD**

801 Application of the LMG method (see Data and Methods section) to the MLR  
802 model allowed the relative contributions of each anthropogenic emission type and  
803 meteorological factor to the inter-decadal variations or trend of regional AOD to be  
804 quantified. Figure 12 shows the relative contributions of the local emissions and





805 meteorological factors to the changes in regional AOD for the period 1980–2014, as  
806 well as for 1980–1997 and 1998–2014, using both emissions and meteorology as  
807 predictors in the MLR model. During the period 1980–2014, over the anthropogenic  
808 aerosol–dominant regions, SO<sub>2</sub> was the dominant emissions driving factor, explaining  
809 24.9%, 15.2%, 32.6%, 21.7% and 12.7% of the variance of AOD over NC, SC, SA,  
810 WEU and the EUS, respectively (also see Table S3). The above results also confirm  
811 that particulate sulfate is the main contributor to fine-mode AOD in anthropogenic  
812 aerosol–dominant regions (Itahashi et al., 2012; David et al., 2018). Meanwhile, wind  
813 speed (including surface and upper wind speed) was the dominant meteorological  
814 driving factor, explaining 11.4%, 14.2% and 17.9% of the variance of AOD over NC,  
815 SC and the EUS, respectively. In addition, planetary boundary layer height,  
816 temperature (including surface temperature, upper temperature, and the temperature  
817 difference between the surface and upper atmosphere) and RH (including surface and  
818 upper RH) were the strongest meteorological driving factors over NEA, SA and WEU,  
819 contributing 30.2%, 15.9% and 21.5%, respectively.

820 On the contrary, over the biomass burning–dominant regions, BC (OC) was the  
821 dominant emissions driving factor over SEA (AMZ), explaining 27.7% (24.0%) of the  
822 variance of AOD. Meanwhile, soil moisture and RH were the top meteorological  
823 driving factors over SEA and AMZ, and CF, contributing 11.7% and 35.5%, and  
824 28.5%, respectively. Furthermore, over the dust-dominant regions, WS was the  
825 strongest meteorological driving factor, explaining 30.3% and 29.8% of the variance  
826 in AOD over NWC and the SD, respectively. Different from WS being the primary  
827 meteorological driving factor over NWC and the SD, it was the second most  
828 important factor over the ME, while sea level pressure was the primary driving factor,  
829 accounting for 60.9% of the variation in AOD. This large variance explained by sea  
830 level pressure and significant anti-correlations of the AOD with it (see Fig. S18c),  
831 further confirms the previous studies' findings that frequent sandstorms over the ME  
832 often correspond to large horizontal pressure gradient differences caused by the  
833 enhanced high-pressure system across the eastern Mediterranean Sea and enhanced  
834 low-pressure system across Iran and Afghanistan (Hamidi et al., 2013; Yu et al.,  
835 2016).

836 By comparing the estimated results of the two independent study periods (i.e.,  
837 1980–1997 and 1998–2014), it was found that in almost all ROIs (except NC and  
838 AMZ), meteorological factors contributed a larger explained proportion of AOD  
839 changes during 1998–2014, which indicates that meteorological factors seem to be  
840 becoming increasingly more important in dominating the inter-decadal change of  
841 regional AOD. It is worth noting that, in addition to the increased explained  
842 proportion of SO<sub>2</sub> and BC, among these meteorological factors, the role of  
843 diffusion-related parameters (such as horizontal and vertical WS, representing  
844 horizontal and vertical diffusion, respectively) seems to be the most prominent. This  
845 is consistent with the findings of Gui et al. (2019), who found WS to be the dominant  
846 meteorological driver for decadal changes in fine particulate matter over SC, based  
847 upon a 19-yr record of satellite-retrieved fine particulate matter data (1998–2016).

848



#### 849 **4 Conclusions and implications**

850 This paper presents a comprehensive assessment of the global and regional AOD  
851 trends over the past 37 years (1980–2016), based on the reanalysis MERRA-2 AOD  
852 dataset. AOD observations from both AERONET and CARSNET stations were used  
853 to assess the performance of the MERRA-2 AOD dataset on global and regional  
854 scales prior to calculating the global and regional AOD trends. Satellite retrievals  
855 from MODIS/Terra and MISR were then used to estimate the AOD annual and  
856 seasonal trends and compare them with the MERRA-2 results. Finally, the stepwise  
857 MLR and LMG methods were jointly applied to quantify the influences of emission  
858 factors and meteorological parameters on the inter-decadal changes in AOD over 12  
859 ROIs during the three periods of 1980–2014, 1980–1997 and 1998–2014.

860 Results showed that the MERRA-2 AOD was comparable in accuracy with the  
861 satellite-retrieved AOD, albeit there was slight underestimation on the global scale  
862 when compared with the in-situ AERONET and CARSNET AOD. MERRA-2 was  
863 proven to be capable of estimating the long-term variability and trend of AOD, owing  
864 to its good accuracy and continuous and complete spatiotemporal resolution. It was  
865 revealed that, in general, MERRA-2 was able to quantitatively reproduce the AOD  
866 annual and seasonal trends (especially decadal trends) during the overlapping years  
867 (2001–2016), as observed by the MODIS/Terra, albeit some discrepancies (caused by  
868 the insufficient sample size) were found when compared to MISR. The resulting trend  
869 analyses based upon the MERRA-2 data from 1980 to 2016 showed that the global  
870 annual trend of AOD during this period, although significantly ( $p < 0.05$ ) weakly  
871 negative (i.e.,  $-0.00068 \text{ yr}^{-1}$ ), was essentially negligible when compared to the  
872 magnitudes of regional AOD trends. On regional scales, sliding trend analyses  
873 suggested that the inter-decadal trends of AOD in different periods could be  
874 significantly different. It was noted that, during the entire study period (1980–2016),  
875 the EUS and WEU showed a non-monotonous decreasing trend accompanied by  
876 occasional fluctuations in the 1980s and 1990s, responding to the decrease in  
877 pollutant emissions, but the intensity of this downward tendency has slowed over the  
878 recent decade. In contrast, AODs in NC and SC experienced a sustained and  
879 significant upward trend before ~2006, and then the trend shifted from upward to  
880 downward due to the Chinese government's emissions-reduction policy. In addition to  
881 the negligible downward trend in the 1980s and 1990s, SA showed overall significant  
882 positive trends throughout the study period. Moreover, the two large volcanic  
883 eruptions that occurred in the 1980s and 1990s not only greatly affected the  
884 short-term changes in local aerosol loading, but also impacted significantly on the  
885 inter-annual trend of the regional AOD around the world. This highlights the  
886 importance of examining the effects of trans-regional pollutant transport on decadal or  
887 temporal shifts in local AOD trends.

888 To diagnose the influences of local anthropogenic emissions and other  
889 meteorological parameters on the inter-decadal variation of regional AODs, statistical  
890 MLR models that estimated AOD monthly values over each ROI as a function of local  
891 emissions factors and various meteorological variables were developed. The modeled



892 AODs using emission factors, meteorological parameters, and both, as input  
893 predictors in the MLR models were compared during three individual periods (i.e.,  
894 1980–2014, 1980–1997 and 1998–2014). In general, the MLR models with both  
895 emissions and meteorological parameters as predictors could account for 42%–76% of  
896 the variability of the MERRA-2 AOD, depending on the ROI. However, when  
897 meteorology and emissions alone were used as predictors, there were considerable  
898 differences in different ROIs. During 1980–2014, compared with the emission factors  
899 (0%–56%), it was found that meteorological parameters explained a larger proportion  
900 of the AOD changes (20.4%–72.8%) over all ROIs (except NC and SEA). Besides,  
901 further analysis also showed that this dominant driving role of meteorological  
902 parameters was stronger during the other two periods.

903 The LMG method for MLR models suggested that SO<sub>2</sub> was the dominant  
904 emissions driving factor, explaining 24.9%, 15.2%, 32.6%, 21.7% and 12.7% of the  
905 variance of AOD over NC, SC, SA, WEU and the EUS, respectively. In contrast, BC  
906 (OC) was the dominant emissions driving factor over SEA (AMZ), explaining 27.7%  
907 (24.0%) of the variance of AOD. For meteorological driving factors, over the mineral  
908 dust–dominant regions, WS was the top driving factor, explaining 30.3% and 29.8%  
909 of the variance of AOD over NWC and the SD. Meanwhile, soil moisture and RH  
910 were the strongest meteorological driving factors over SEA and AMZ, and CF,  
911 contributing 11.7% and 35.5%, and 28.5%, respectively. Notably, the performance of  
912 the MLR model in 1980–1997 was significantly worse than that in 1998–2014, which  
913 can mainly be attributed to the fact that the statistical model used in this study did not  
914 take into account the impact of trans-regional transport. Consequently, the model  
915 failed to capture the abnormally high values of regional AOD caused by trans-regional  
916 transport during 1980–1997. Finally, deeper insight into the influence of emissions  
917 and meteorological factors, as well as the influence of atmospheric transport, on the  
918 inter-decadal change in regional AOD, will be provided in future modeling studies.

919

### 920 **Data availability:**

921 The CARSNET AOD dataset used in the study can be requested by contacting the  
922 corresponding author.

923

### 924 **Competing interests:**

925 The authors declare that they have no conflict of interest.

926

### 927 **Author contribution:**

928 All authors contributed to shaping up the ideas and reviewing the paper. HC, KG and  
929 XZ designed and implemented the research, as well as prepared the manuscript; HC,  
930 KG and YW contributed to analysis of the MERRA-2, MODIS and MISR dataset; HC,  
931 XX, BNH, PG, and EGA contributed to the CARSNET data retrieval; HC, KG, YW,  
932 HW, YZ, and HZ carried out the CARSNET observations; XX, BNH, PG, and EGA



933 provided constructive comments on this research

934

### 935 **Acknowledgements:**

936 This work was supported by grants from the National Science Fund for Distinguished  
937 Young Scholars (41825011), the National Key R & D Program Pilot Projects of China  
938 (2016YFA0601901 and 2016YFC0203304), National Natural Science Foundation of  
939 China (41590874), the CAMS Basis Research Project (2017Z011), the European  
940 Union Seventh Framework Programme (FP7/2007-2013) under grant agreement no.  
941 262254, and the AERONET-Europe ACTRIS-2 program, European Union's Horizon  
942 2020 research and innovation programme under grant agreement no. 654109. NASA's  
943 global modeling and assimilation office is gratefully acknowledged for making the  
944 MERRA-2 aerosol reanalysis publicly accessible  
945 (<https://disc.gsfc.nasa.gov/daac-bin/FTPSubset2.pl>). Thanks are also extended to the  
946 PKU emissions inventory research group (<http://inventory.pku.edu.cn/home.html>) and  
947 AERONET networks (<https://aeronet.gsfc.nasa.gov/>) for making their data available  
948 online, as well as the GES-DISC for providing gridded AOD products of MODIS and  
949 MISR through their Giovanni website (<https://giovanni.gsfc.nasa.gov/giovanni/>).

950

### 951 **References**

- 952 Ackerman, A. S., Toon, O. B., Stevens, D. E., Heymsfield, A. J., Ramanathan, V. and  
953 Welton, E. J.: Reduction of tropical cloudiness by soot, *Science*, 288(5468),  
954 1042-1047, doi:10.1126/science.288.5468.1042, 2000.
- 955 Altland, H. W., Freund, R. J. and Wilson, W. J.: Regression Analysis: Statistical  
956 Modeling of a Response Variable, *Technometrics*, doi:10.2307/1271353, 2006.
- 957 An, L., Che, H., Xue, M., Zhang, T., Wang, H., Wang, Y., Zhou, C., Zhao, H., Gui,  
958 K., Zheng, Y., Sun, T., Liang, Y., Sun, E., Zhang, H. and Zhang, X.: Temporal and  
959 spatial variations in sand and dust storm events in East Asia from 2007 to 2016:  
960 Relationships with surface conditions and climate change, *Sci. Total Environ.*, 633,  
961 doi:10.1016/j.scitotenv.2018.03.068, 2018.
- 962 Andreae, M. O.: Correlation between cloud condensation nuclei concentration and  
963 aerosol optical thickness in remote and polluted regions, *Atmos. Chem. Phys.*,  
964 doi:10.5194/acp-9-543-2009, 2009.
- 965 Barnett, V., Neter, J. and Wasserman, W.: *Applied Linear Statistical Models.*, J. R.  
966 Stat. Soc. Ser. A, doi:10.2307/2984653, 2006.
- 967 Bi, J.: A review of statistical methods for determination of relative importance of  
968 correlated predictors and identification of drivers of consumer liking, *J. Sens. Stud.*,  
969 27(2), 87–101, doi:10.1111/j.1745-459X.2012.00370.x, 2012.
- 970 Bluth, G. J. S., Doiron, S. D., Schnetzler, C. C., Krueger, A. J. and Walter, L. S.:  
971 Global tracking of the SO<sub>2</sub> clouds from the June, 1991 Mount Pinatubo eruptions,  
972 *Geophys. Res. Lett.*, doi:10.1029/91GL02792, 1992.
- 973 Buchard, V., Randles, C. A., da Silva, A. M., Darmenov, A., Colarco, P. R.,



- 974 Govindaraju, R., Ferrare, R., Hair, J., Beyersdorf, A. J., Ziemba, L. D. and Yu, H.:  
975 The MERRA-2 aerosol reanalysis, 1980 onward. Part II: Evaluation and case  
976 studies, *J. Clim.*, 30(17), 6851–6872, doi:10.1175/JCLI-D-16-0613.1, 2017.
- 977 Che, H., Zhang, X., Li, Y., Zhou, Z. and Qu, J. J.: Horizontal visibility trends in China  
978 1981–2005, *Geophys. Res. Lett.*, 34(24), 1–5, doi:10.1029/2007GL031450, 2007.
- 979 Che, H., Zhang, X., Chen, H., Damiri, B., Goloub, P., Li, Z., Zhang, X., Wei, Y.,  
980 Zhou, H., Dong, F., Li, D. and Zhou, T.: Instrument calibration and aerosol optical  
981 depth validation of the China aerosol remote sensing network, *J. Geophys. Res.*  
982 *Atmos.*, doi:10.1029/2008JD011030, 2009.
- 983 Che, H., Xia, X., Zhu, J., Li, Z., Dubovik, O., Holben, B., Goloub, P., Chen, H.,  
984 Estelles, V., Cuevas-Agulló E., Blarel, L., Wang, H., Zhao, H., Zhang, X., Wang,  
985 Y., Sun, J., Tao, R., Zhang, X. and Shi, G.: Column aerosol optical properties and  
986 aerosol radiative forcing during a serious haze-fog month over North China Plain  
987 in 2013 based on ground-based sunphotometer measurements, *Atmos. Chem. Phys.*,  
988 14(4), 2125–2138, doi:10.5194/acp-14-2125-2014, 2014.
- 989 Che, H., Zhang, X. Y., Xia, X., Goloub, P., Holben, B., Zhao, H., Wang, Y., Zhang, X.  
990 C., Wang, H., Blarel, L., Damiri, B., Zhang, R., Deng, X., Ma, Y., Wang, T., Geng,  
991 F., Qi, B., Zhu, J., Yu, J., Chen, Q. and Shi, G.: Ground-based aerosol climatology  
992 of China: Aerosol optical depths from the China Aerosol Remote Sensing Network  
993 (CARSNET) 2002–2013, *Atmos. Chem. Phys.*, 15(13), 7619–7652,  
994 doi:10.5194/acp-15-7619-2015, 2015.
- 995 Che, H., Qi, B., Zhao, H., Xia, X., Eck, T. F., Goloub, P., Dubovik, O., Estelles, V.,  
996 Cuevas-Agulló E., Blarel, L., Wu, Y., Zhu, J., Du, R., Wang, Y., Wang, H., Gui,  
997 K., Yu, J., Zheng, Y., Sun, T., Chen, Q., Shi, G. and Zhang, X.: Aerosol optical  
998 properties and direct radiative forcing based on measurements from the China  
999 Aerosol Remote Sensing Network (CARSNET) in eastern China, *Atmos. Chem.*  
1000 *Phys.*, 18(1), 405–425, doi:10.5194/acp-18-405-2018, 2018.
- 1001 Chen, J., Li, C., Ristovski, Z., Milic, A., Gu, Y., Islam, M. S., Wang, S., Hao, J.,  
1002 Zhang, H., He, C., Guo, H., Fu, H., Miljevic, B., Morawska, L., Thai, P., LAM, Y.  
1003 F., Pereira, G., Ding, A., Huang, X. and Dumka, U. C.: A review of biomass  
1004 burning: Emissions and impacts on air quality, health and climate in China, *Sci.*  
1005 *Total Environ.*, doi:10.1016/j.scitotenv.2016.11.025, 2017.
- 1006 Chin, M., Ginoux, P., Kinne, S., Torres, O., Holben, B. N., Duncan, B. N., Martin, R.  
1007 V., Logan, J. A., Higurashi, A. and Nakajima, T.: Tropospheric Aerosol Optical  
1008 Thickness from the GOCART Model and Comparisons with Satellite and Sun  
1009 Photometer Measurements, *J. Atmos. Sci.*, 59(3), 461–483,  
1010 doi:10.1175/1520-0469(2002)059<0461:TAOTFT>2.0.CO;2, 2002.
- 1011 Chin, M., Diehl, T., Tan, Q., Prospero, J. M., Kahn, R. A., Remer, L. A., Yu, H.,  
1012 Sayer, A. M., Bian, H., Geogdzhayev, I. V., Holben, B. N., Howell, S. G., Huebert,  
1013 B. J., Hsu, N. C., Kim, D., Kucsera, T. L., Levy, R. C., Mishchenko, M. I., Pan, X.,  
1014 Quinn, P. K., Schuster, G. L., Streets, D. G., Strode, S. A. and Torres, O.:  
1015 Multi-decadal aerosol variations from 1980 to 2009: A perspective from  
1016 observations and a global model, *Atmos. Chem. Phys.*, 14(7), 3657–3690,  
1017 doi:10.5194/acp-14-3657-2014, 2014.



- 1018 Cohen, A. J., Brauer, M., Burnett, R., Anderson, H. R., Frostad, J., Estep, K.,  
1019 Balakrishnan, K., Brunekreef, B., Dandona, L., Dandona, R., Feigin, V., Freedman,  
1020 G., Hubbell, B., Jobling, A., Kan, H., Knibbs, L., Liu, Y., Martin, R., Morawska, L.,  
1021 Pope, C. A., Shin, H., Straif, K., Shaddick, G., Thomas, M., van Dingenen, R., van  
1022 Donkelaar, A., Vos, T., Murray, C. J. L. and Forouzanfar, M. H.: Estimates and  
1023 25-year trends of the global burden of disease attributable to ambient air pollution:  
1024 an analysis of data from the Global Burden of Diseases Study 2015, *Lancet*,  
1025 389(10082), 1907–1918, doi:10.1016/S0140-6736(17)30505-6, 2017.
- 1026 Colarco, P., Da Silva, A., Chin, M. and Diehl, T.: Online simulations of global aerosol  
1027 distributions in the NASA GEOS-4 model and comparisons to satellite and  
1028 ground-based aerosol optical depth, *J. Geophys. Res. Atmos.*, 115(14),  
1029 doi:10.1029/2009JD012820, 2010.
- 1030 David, L. M., Ravishankara, A. R., Kodros, J. K., Venkataraman, C., Sadavarte, P.,  
1031 Pierce, J. R., Chaliyakunnel, S. and Millet, D. B.: Aerosol Optical Depth Over  
1032 India, *J. Geophys. Res. Atmos.*, doi:10.1002/2017JD027719, 2018.
- 1033 Diner, D. J., Beckert, J. C., Reilly, T. H., Bruegge, C. J., Conel, J. E., Kahn, R. A.,  
1034 Martonchik, J. V., Ackerman, T. P., Davies, R., Gerstl, S. A. W., Gordon, H. R.,  
1035 Muller, J. P., Myneni, R. B., Sellers, P. J., Pinty, B. and Verstraete, M. M.:  
1036 Multi-angle imaging spectroradiometer (MISR) instrument description and  
1037 experiment overview, *IEEE Trans. Geosci. Remote Sens.*, 36(4), 1072–1087,  
1038 doi:10.1109/36.700992, 1998.
- 1039 Eck, T. F., Holben, B. N., Reid, J. S., Dubovik, O., Smirnov, A., O'Neill, N. T.,  
1040 Slutsker, I. and Kinne, S.: Wavelength dependence of the optical depth of biomass  
1041 burning, urban, and desert dust aerosols, *J. Geophys. Res.*,  
1042 doi:10.1029/1999JD900923, 1999.
- 1043 Edgar: EDGAR - Emission Database for Global Atmospheric Research, *Glob. Emiss.*  
1044 EDGAR v4.2 (November 2011), doi:10.2904/EDGARv4.2, 2011.
- 1045 Fan, A., Chen, W., Liang, L., Sun, W., Lin, Y., Che, H. and Zhao, X.: Evaluation and  
1046 comparison of long-term MODIS C5.1 and C6 products against AERONET  
1047 observations over China, *Remote Sens.*, 9(12), 1–16, doi:10.3390/rs9121269, 2017.
- 1048 Feng, Y., Chen, D., Ouyang, X. and Zhang, X.: Variability of satellite-based total  
1049 aerosols and the relationship with emission, meteorology and landscape in North  
1050 China during 2000–2016, *Environ. Earth Sci.*, 77(13), 1–11,  
1051 doi:10.1007/s12665-018-7685-y, 2018.
- 1052 Field, A.: *Discovering Statistics Using SPSS*, 2005.
- 1053 Gao, M., Ji, D., Liang, F. and Liu, Y.: Attribution of aerosol direct radiative forcing in  
1054 China and India to emitting sectors, *Atmos. Environ.*, 190, 35–42,  
1055 doi:10.1016/j.atmosenv.2018.07.011, 2018.
- 1056 Gelaro, R., McCarty, W., Suárez, M. J., Todling, R., Molod, A., Takacs, L., Randles,  
1057 C. A., Darmenov, A., Bosilovich, M. G., Reichle, R., Wargan, K., Coy, L.,  
1058 Cullather, R., Draper, C., Akella, S., Buchard, V., Conaty, A., da Silva, A. M., Gu,  
1059 W., Kim, G. K., Koster, R., Lucchesi, R., Merkova, D., Nielsen, J. E., Partyka, G.,  
1060 Pawson, S., Putman, W., Rienecker, M., Schubert, S. D., Sienkiewicz, M. and Zhao,  
1061 B.: The modern-era retrospective analysis for research and applications, version 2





- 1062 (MERRA-2), *J. Clim.*, 30(14), 5419–5454, doi:10.1175/JCLI-D-16-0758.1, 2017.
- 1063 Goldammer, J. G.: History of equatorial vegetation fires and fire research in Southeast  
1064 Asia before the 1997-98 episode: A reconstruction of creeping environmental  
1065 changes, *Mitig. Adapt. Strateg. Glob. Chang.*, doi:10.1007/s11027-006-9044-7,  
1066 2007.
- 1067 Grömping, U.: Relative importance for linear regression in R: the package relaimpo, *J.*  
1068 *Stat. Softw.*, doi:10.1016/j.foreco.2006.08.245, 2006.
- 1069 Gui, K., Che, H., Wang, Y., Wang, H., Zhang, L., Zhao, H., Zheng, Y., Sun, T. and  
1070 Zhang, X.: Satellite-derived PM<sub>2.5</sub> concentration trends over Eastern China from  
1071 1998 to 2016: Relationships to emissions and meteorological, *Environ. Pollut.*, 247,  
1072 1125–1133, doi:10.1016/j.envpol.2019.01.056, 2019.
- 1073 Hair, J. F., Black, W. C., Babin, B. J. and Anderson, R. E.: *Multivariate Data Analysis*  
1074 (7th Edition), 2010.
- 1075 Hamidi, M., Kavianpour, M. R. and Shao, Y.: Synoptic analysis of dust storms in the  
1076 Middle East, *Asia-Pacific J. Atmos. Sci.*, 49(3), 279–286,  
1077 doi:10.1007/s13143-013-0027-9, 2013.
- 1078 Hammer, M. S., Martin, R. V., Li, C., Torres, O., Manning, M. and Boys, B. L.:  
1079 Insight into global trends in aerosol composition from 2005 to 2015 inferred from  
1080 the OMI Ultraviolet Aerosol Index, *Atmos. Chem. Phys.*, 18(11), 8097–8112,  
1081 doi:10.5194/acp-18-8097-2018, 2018
- 1082 Hansen, J., Sato, M. and Ruedy, R.: Radiative forcing and climate response, *J.*  
1083 *Geophys. Res. Atmos.*, doi:10.1029/96JD03436, 1997.
- 1084 He, Q., Zhang, M. and Huang, B.: Spatio-temporal variation and impact factors  
1085 analysis of satellite-based aerosol optical depth over China from 2002 to 2015,  
1086 *Atmos. Environ.*, 129, 79–90, doi:10.1016/j.atmosenv.2016.01.002, 2016.
- 1087 Heidinger, A. K., Foster, M. J., Walther, A. and Zhao, X.: The pathfinder  
1088 atmospheres-extended avhrr climate dataset, *Bull. Am. Meteorol. Soc.*, 95(6), 909–  
1089 922, doi:10.1175/BAMS-D-12-00246.1, 2014.
- 1090 Hofmann, D. J. and Rosen, J. M.: Stratospheric sulfuric acid fraction and mass  
1091 estimate for the 1982 volcanic eruption of El Chichon, *Geophys. Res. Lett.*,  
1092 doi:10.1029/GL010i004p00313, 1983.
- 1093 Holben, B. N., Eck, T. F., Slutsker, I., Tanré D., Buis, J. P., Setzer, A., Vermote, E.,  
1094 Reagan, J. A., Kaufman, Y. J., Nakajima, T., Lavenu, F., Jankowiak, I. and  
1095 Smirnov, A.: AERONET—A Federated Instrument Network and Data Archive for  
1096 Aerosol Characterization, *Remote Sens. Environ.*, 66(1), 1–16,  
1097 doi:10.1016/S0034-4257(98)00031-5, 1998.
- 1098 Hsu, N. C., Gautam, R., Sayer, A. M., Bettenhausen, C., Li, C., Jeong, M. J., Tsay, S.  
1099 C. and Holben, B. N.: Global and regional trends of aerosol optical depth over land  
1100 and ocean using SeaWiFS measurements from 1997 to 2010, *Atmos. Chem. Phys.*,  
1101 12(17), 8037–8053, doi:10.5194/acp-12-8037-2012, 2012.
- 1102 Huang, Y., Shen, H., Chen, H., Wang, R., Zhang, Y., Su, S., Chen, Y., Lin, N., Zhuo,  
1103 S., Zhong, Q., Wang, X., Liu, J., Li, B., Liu, W. and Tao, S.: Quantification of  
1104 global primary emissions of PM<sub>2.5</sub>, PM<sub>10</sub>, and TSP from combustion and industrial  
1105 process sources, *Environ. Sci. Technol.*, doi:10.1021/es503696k, 2014.



- 1106 Huang, Y., Shen, H., Chen, Y., Zhong, Q., Chen, H., Wang, R., Shen, G., Liu, J., Li,  
1107 B. and Tao, S.: Global organic carbon emissions from primary sources from 1960  
1108 to 2009, *Atmos. Environ.*, 122, 505–512, doi:10.1016/j.atmosenv.2015.10.017,  
1109 2015.
- 1110 Ikemori, F., Sugata, S., Uranishi, K., Shimadera, H. and Kondo, A.: Impact of field  
1111 biomass burning on local pollution and long-range transport of PM<sub>2.5</sub> in Northeast  
1112 Asia, *Environ. Pollut.*, 244, 414–422, doi:10.1016/j.envpol.2018.09.061, 2018.
- 1113 IPCC: IPCC Fourth Assessment Report: Climate Change 2007., 2007.
- 1114 Itahashi, S., Uno, I., Yumimoto, K., Irie, H., Osada, K., Ogata, K., Fukushima, H.,  
1115 Wang, Z. and Ohara, T.: Interannual variation in the fine-mode MODIS aerosol  
1116 optical depth and its relationship to the changes in sulfur dioxide emissions in  
1117 China between 2000 and 2010, *Atmos. Chem. Phys.*, 12(5), 2631–2640,  
1118 doi:10.5194/acp-12-2631-2012, 2012.
- 1119 Jiang, J. H., Su, H., Huang, L., Wang, Y., Massie, S., Zhao, B., Omar, A. and Wang,  
1120 Z.: Contrasting effects on deep convective clouds by different types of aerosols,  
1121 *Nat. Commun.*, 9(1), 3874, doi:10.1038/s41467-018-06280-4, 2018.
- 1122 Kahn, R. A., Gaitley, B. J., Martonchik, J. V., Diner, D. J., Crean, K. A. and Holben,  
1123 B.: Multiangle Imaging Spectroradiometer (MISR) global aerosol optical depth  
1124 validation based on 2 years of coincident Aerosol Robotic Network (AERONET)  
1125 observations, *J. Geophys. Res. D Atmos.*, 110(10), 1–16,  
1126 doi:10.1029/2004JD004706, 2005.
- 1127 Kahn, R. A., Nelson, D. L., Garay, M. J., Levy, R. C., Bull, M. A., Diner, D. J.,  
1128 Martonchik, J. V., Paradise, S. R., Hansen, E. G. and Remer, L. A.: MISR aerosol  
1129 product attributes and statistical comparisons with MODIS, *IEEE Trans. Geosci.*  
1130 *Remote Sens.*, doi:10.1109/TGRS.2009.2023115, 2009.
- 1131 Kahn, R. A., Gaitley, B. J., Garay, M. J., Diner, D. J., Eck, T. F., Smirnov, A. and  
1132 Holben, B. N.: Multiangle Imaging SpectroRadiometer global aerosol product  
1133 assessment by comparison with the Aerosol Robotic Network, *J. Geophys. Res.*  
1134 *Atmos.*, 115(23), doi:10.1029/2010JD014601, 2010.
- 1135 Kim, D., Chin, M., Remer, L. A., Diehl, T., Bian, H., Yu, H., Brown, M. E. and  
1136 Stockwell, W. R.: Role of surface wind and vegetation cover in multi-decadal  
1137 variations of dust emission in the Sahara and Sahel, *Atmos. Environ.*,  
1138 doi:10.1016/j.atmosenv.2016.10.051, 2017.
- 1139 King, M. D., Menzel, W. P., Kaufman, Y. J., Tanré D., Gao, B. C., Platnick, S.,  
1140 Ackerman, S. A., Remer, L. A., Pincus, R. and Hubanks, P. A.: Cloud and aerosol  
1141 properties, precipitable water, and profiles of temperature and water vapor from  
1142 MODIS, *IEEE Trans. Geosci. Remote Sens.*, 41, 442–456,  
1143 doi:10.1109/TGRS.2002.808226, 2003.
- 1144 Kirchner, I., Stenchikov, G. L., Graf, H. F., Robock, A. and Antuña, J. C.: Climate  
1145 model simulation of winter warming and summer cooling following the 1991  
1146 Mount Pinatubo volcanic eruption, *J. Geophys. Res. Atmos.*,  
1147 doi:10.1029/1999JD900213, 1999.
- 1148 Klingmüller, K., Pozzer, A., Metzger, S., Stenchikov, G. L. and Lelieveld, J.: Aerosol  
1149 optical depth trend over the Middle East, *Atmos. Chem. Phys.*, 16(8), 5063–5073,



- 1150 doi:10.5194/acp-16-5063-2016, 2016.
- 1151 De Leeuw, G., Sogacheva, L., Rodriguez, E., Kourtidis, K., Georgoulas, A. K.,  
1152 Alexandri, G., Amiridis, V., Proestakis, E., Marinou, E., Xue, Y. and Van Der A,  
1153 R.: Two decades of satellite observations of AOD over mainland China using  
1154 ATSR-2, AATSR and MODIS/Terra: Data set evaluation and large-scale patterns,  
1155 Atmos. Chem. Phys., 18(3), 1573–1592, doi:10.5194/acp-18-1573-2018, 2018.
- 1156 Lelieveld, J., Evans, J. S., Fnais, M., Giannadaki, D. and Pozzer, A.: The contribution  
1157 of outdoor air pollution sources to premature mortality on a global scale, Nature,  
1158 525(7569), 367–371, doi:10.1038/nature15371, 2015.
- 1159 Levy, R. C., Remer, L. A., Kleidman, R. G., Mattoo, S., Ichoku, C., Kahn, R. and Eck,  
1160 T. F.: Global evaluation of the Collection 5 MODIS dark-target aerosol products  
1161 over land, Atmos. Chem. Phys., 10(21), 10399–10420,  
1162 doi:10.5194/acp-10-10399-2010, 2010.
- 1163 Levy, R. C., Mattoo, S., Munchak, L. A., Remer, L. A., Sayer, A. M., Patadia, F. and  
1164 Hsu, N. C.: The Collection 6 MODIS aerosol products over land and ocean, Atmos.  
1165 Meas. Tech., 6(11), 2989–3034, doi:10.5194/amt-6-2989-2013, 2013.
- 1166 Levy, R. C., Munchak, L. A., Mattoo, S., Patadia, F., Remer, L. A. and Holz, R. E.:  
1167 Towards a long-term global aerosol optical depth record: Applying a consistent  
1168 aerosol retrieval algorithm to MODIS and VIIRS-observed reflectance, Atmos.  
1169 Meas. Tech., 8(10), 4083–4110, doi:10.5194/amt-8-4083-2015, 2015.
- 1170 Li, J., Carlson, B. E., Dubovik, O. and Laciš, A. A.: Recent trends in aerosol optical  
1171 properties derived from AERONET measurements, Atmos. Chem. Phys., 14(22),  
1172 12271–12289, doi:10.5194/acp-14-12271-2014, 2014.
- 1173 Lindeman, R. H., Merenda, P. F. and Gold, R. Z.: Introduction to Bivariate and  
1174 Multivariate Analysis., Scott, Foresman, Glenview, Ill., 76(375), 2014.
- 1175 Liu, J., Röhland, K. M., Chen, J., Xu, Y., Chen, S., Chen, Q., Huang, W., Xu, Q.,  
1176 Chen, F. and Smol, J. P.: Aerosol-weakened summer monsoons decrease lake  
1177 fertilization on the Chinese Loess Plateau, Nat. Clim. Chang., 7(3), 190–194,  
1178 doi:10.1038/nclimate3220, 2017.
- 1179 Ma, Z., Hu, X., Sayer, A. M., Levy, R., Zhang, Q., Xue, Y., Tong, S., Bi, J., Huang, L.  
1180 and Liu, Y.: Satellite-based spatiotemporal trends in PM<sub>2.5</sub> concentrations: China,  
1181 2004–2013, Environ. Health Perspect., 124(2), 184–192, doi:10.1289/ehp.1409481,  
1182 2016.
- 1183 McCormick, R. A. and Ludwig, J. H.: Climate modification by atmospheric aerosols,  
1184 Science, 156(3780), 1358–1359, doi:10.1126/science.156.3780.1358, 1967.
- 1185 Mehta, M., Singh, R., Singh, A., Singh, N. and Anshumali: Recent global aerosol  
1186 optical depth variations and trends - A comparative study using MODIS and MISR  
1187 level 3 datasets, Remote Sens. Environ., 181, 137–150,  
1188 doi:10.1016/j.rse.2016.04.004, 2016.
- 1189 Meij, A. De, Pozzer, A. and Lelieveld, J.: Trend analysis in aerosol optical depths and  
1190 pollutant emission estimates between 2000 and 2009, Atmos. Environ., 51, 75–85,  
1191 doi:10.1016/j.atmosenv.2012.01.059, 2012.
- 1192 De Meij, A., Pozzer, A. and Lelieveld, J.: Trend analysis in aerosol optical depths and  
1193 pollutant emission estimates between 2000 and 2009, Atmos. Environ., 51, 75–85,



- 1194 doi:10.1016/j.atmosenv.2012.01.059, 2012.
- 1195 Minguillón, M. C., Brines, M., Pérez, N., Reche, C., Pandolfi, M., Fonseca, A. S.,  
1196 Amato, F., Alastuey, A., Llyasota, A., Codina, B., Lee, H. K., Eun, H. R., Ahn, K.  
1197 H. and Querol, X.: New particle formation at ground level and in the vertical  
1198 column over the Barcelona area, *Atmos. Res.*, doi:10.1016/j.atmosres.2015.05.003,  
1199 2015.
- 1200 Molod, A., Takacs, L., Suarez, M., Bacmeister, J., Song, I.-S. and Eichmann, A.: The  
1201 GEOS-5 atmospheric general circulation model: Mean climate and development  
1202 from MERRA to Fortuna., 2012.
- 1203 Molod, A., Takacs, L., Suarez, M. and Bacmeister, J.: Development of the GEOS-5  
1204 atmospheric general circulation model: Evolution from MERRA to MERRA2,  
1205 *Geosci. Model Dev.*, 8(5), 1339–1356, doi:10.5194/gmd-8-1339-2015, 2015.
- 1206 Page, S. E., Siegert, F., Rieley, J. O., Boehm, H. D. V., Jaya, A. and Limin, S.: The  
1207 amount of carbon released from peat and forest fires in Indonesia during 1997,  
1208 *Nature*, doi:10.1038/nature01131, 2002.
- 1209 Pozzer, A., De Meij, A., Yoon, J., Tost, H., Georgoulias, A. K. and Astitha, M.: AOD  
1210 trends during 2001–2010 from observations and model simulations, *Atmos. Chem.*  
1211 *Phys.*, 15(10), 5521–5535, doi:10.5194/acp-15-5521-2015, 2015.
- 1212 Qin, W., Liu, Y., Wang, L., Lin, A., Xia, X., Che, H., Bilal, M., Zhang, M., Qin, W.,  
1213 Liu, Y., Wang, L., Lin, A., Xia, X., Che, H., Bilal, M. and Zhang, M.:  
1214 Characteristic and Driving Factors of Aerosol Optical Depth over Mainland China  
1215 during 1980–2017, *Remote Sens.*, 10(7), 1064, doi:10.3390/rs10071064, 2018.
- 1216 Ramanathan, V., Crutzen, P. J., Kiehl, J. T. and Rosenfeld, D.: Atmosphere: Aerosols,  
1217 climate, and the hydrological cycle, *Science*, 294(5549), 2119–2124,  
1218 doi:10.1126/science.1064034, 2001.
- 1219 Remer, L. A., Kaufman, Y. J., Tanré D., Mattoo, S., Chu, D. A., Martins, J. V., Li,  
1220 R.-R., Ichoku, C., Levy, R. C., Kleidman, R. G., Eck, T. F., Vermote, E. and  
1221 Holben, B. N.: The MODIS Aerosol Algorithm, Products, and Validation, *J. Atmos.*  
1222 *Sci.*, 62(4), 947–973, doi:10.1175/JAS3385.1, 2005.
- 1223 Rosenfeld, D., Zhu, Y., Wang, M., Zheng, Y., Goren, T. and Yu, S.: Aerosol-driven  
1224 droplet concentrations dominate coverage and water of oceanic low-level clouds,  
1225 *Science*, 363(6427), eaav0566, doi:10.1126/science.aav0566, 2019.
- 1226 Sarangi, C., Kanawade, V. P., Tripathi, S. N., Thomas, A. and Ganguly, D.:  
1227 Aerosol-induced intensification of cooling effect of clouds during Indian summer  
1228 monsoon, *Nat. Commun.*, 9(1), doi:10.1038/s41467-018-06015-5, 2018.
- 1229 Silva, R. A., West, J. J., Zhang, Y., Anenberg, S. C., Lamarque, J. F., Shindell, D. T.,  
1230 Collins, W. J., Dalsoren, S., Faluvegi, G., Folberth, G., Horowitz, L. W.,  
1231 Nagashima, T., Naik, V., Rumbold, S., Skeie, R., Sudo, K., Takemura, T.,  
1232 Bergmann, D., Cameron-Smith, P., Cionni, I., Doherty, R. M., Eyring, V., Josse, B.,  
1233 Mackenzie, I. A., Plummer, D., Righi, M., Stevenson, D. S., Strode, S., Szopa, S.  
1234 and Zeng, G.: Global premature mortality due to anthropogenic outdoor air  
1235 pollution and the contribution of past climate change, *Environ. Res. Lett.*,  
1236 doi:10.1088/1748-9326/8/3/034005, 2013.
- 1237 Smirnov, A., Holben, B. N., Eck, T. F., Dubovik, O. and Slutsker, I.: Cloud-screening



- 1238 and quality control algorithms for the AERONET database, *Remote Sens. Environ.*,  
1239 doi:10.1016/S0034-4257(00)00109-7, 2000.
- 1240 Song, Z., Fu, D., Zhang, X., Wu, Y., Xia, X. and He, J.: Diurnal and seasonal  
1241 variability of PM<sub>2.5</sub> and AOD in North China plain : Comparison of MERRA-2  
1242 products and ground measurements, *Atmos. Environ.*, 191, 70–78,  
1243 doi:10.1016/j.atmosenv.2018.08.012, 2018.
- 1244 Stenchikov, G. L., Kirchner, I., Robock, A., Graf, H. F., Antuña, J. C., Grainger, R. G.,  
1245 Lambert, A. and Thomason, L.: Radiative forcing from the 1991 Mount Pinatubo  
1246 volcanic eruption, *J. Geophys. Res. Atmos.*, doi:10.1029/98JD00693, 1998.
- 1247 Su, S., Li, B., Cui, S. and Tao, S.: Sulfur dioxide emissions from combustion in China:  
1248 From 1990 to 2007, *Environ. Sci. Technol.*, 45(19), 8403–8410,  
1249 doi:10.1021/es201656f, 2011.
- 1250 Sun, T., Che, H., Qi, B., Wang, Y., Dong, Y., Xia, X., Wang, H., Gui, K., Zheng, Y.,  
1251 Zhao, H., Ma, Q., Du, R. and Zhang, X.: Aerosol optical characteristics and their  
1252 vertical distributions under enhanced haze pollution events: Effect of the regional  
1253 transport of different aerosol types over eastern China, *Atmos. Chem. Phys.*, 18(4),  
1254 doi:10.5194/acp-18-2949-2018, 2018.
- 1255 Tai, A. P. K., Mickley, L. J. and Jacob, D. J.: Correlations between fine particulate  
1256 matter (PM<sub>2.5</sub>) and meteorological variables in the United States: Implications for  
1257 the sensitivity of PM<sub>2.5</sub> to climate change, *Atmos. Environ.*,  
1258 doi:10.1016/j.atmosenv.2010.06.060, 2010.
- 1259 Thornhill, G. D., Ryder, C. L., Highwood, E. J., Shaffrey, L. C. and Johnson, B. T.:  
1260 The effect of South American biomass burning aerosol emissions on the regional  
1261 climate, *Atmos. Chem. Phys.*, doi:10.5194/acp-18-5321-2018, 2018.
- 1262 Tummon, F., Solmon, F., Liousse, C. and Tadrass, M.: Simulation of the direct and  
1263 semidirect aerosol effects on the southern Africa regional climate during the  
1264 biomass burning season, *J. Geophys. Res. Atmos.*, doi:10.1029/2009JD013738,  
1265 2010.
- 1266 Wang, K., Dickinson, R. E. and Liang, S.: Clear sky visibility has decreased over land  
1267 globally from 1973 to 2007, *Science*, 323(5920), 1468–1470,  
1268 doi:10.1126/science.1167549, 2009.
- 1269 Wang, R., Tao, S., Shen, H., Huang, Y., Chen, H., Balkanski, Y., Boucher, O., Ciais,  
1270 P., Shen, G., Li, W., Zhang, Y., Chen, Y., Lin, N., Su, S., Li, B., Liu, J. and Liu,  
1271 W.: Trend in global black carbon emissions from 1960 to 2007, *Environ. Sci.*  
1272 *Technol.*, 48(12), 6780–6787, doi:10.1021/es5021422, 2014.
- 1273 Wang, X., Liu, J., Che, H., Ji, F. and Liu, J.: Spatial and temporal evolution of natural  
1274 and anthropogenic dust events over northern China, *Sci. Rep.*, 8(1),  
1275 doi:10.1038/s41598-018-20382-5, 2018.
- 1276 Yang, Y., Liao, H. and Lou, S.: Increase in winter haze over eastern China in recent  
1277 decades: Roles of variations in meteorological parameters and anthropogenic  
1278 emissions, *J. Geophys. Res.*, 121(21), 13,050–13,065, doi:10.1002/2016JD025136,  
1279 2016.
- 1280 Yu, Y., Notaro, M., Kalashnikova, O. V. and Garay, M. J.: Climatology of summer  
1281 Shamal wind in the Middle East, *J. Geophys. Res.*, doi:10.1002/2015JD024063,



- 1282 2016.
- 1283 Yue, X., Unger, N., Harper, K., Xia, X., Liao, H., Zhu, T., Xiao, J., Feng, Z. and Li, J.:
- 1284 Ozone and haze pollution weakens net primary productivity in China, Atmos.
- 1285 Chem. Phys., 17(9), 6073–6089, doi:10.5194/acp-17-6073-2017, 2017.
- 1286 Zhang, H., Shen, Z., Wei, X., Zhang, M. and Li, Z.: Comparison of optical properties
- 1287 of nitrate and sulfate aerosol and the direct radiative forcing due to nitrate in China,
- 1288 Atmos. Res., doi:10.1016/j.atmosres.2012.04.020, 2012.
- 1289 Zhang, J. and Reid, J. S.: A decadal regional and global trend analysis of the aerosol
- 1290 optical depth using a data-assimilation grade over-water MODIS and Level 2
- 1291 MISR aerosol products, Atmos. Chem. Phys., 10(22), 10949–10963,
- 1292 doi:10.5194/acp-10-10949-2010, 2010.
- 1293 Zhao, B., Jiang, J. H., Gu, Y., Diner, D., Worden, J., Liou, K. N., Su, H., Xing, J.,
- 1294 Garay, M. and Huang, L.: Decadal-scale trends in regional aerosol particle
- 1295 properties and their linkage to emission changes, Environ. Res. Lett., 12(5),
- 1296 doi:10.1088/1748-9326/aa6cb2, 2017.
- 1297 Zhao, B., Jiang, J. H., Diner, D. J., Su, H., Gu, Y., Liou, K.-N., Jiang, Z., Huang, L.,
- 1298 Takano, Y., Fan, X. and Omar, A. H.: Intra-annual variations of regional aerosol
- 1299 optical depth, vertical distribution, and particle types from multiple satellite and
- 1300 ground-based observational datasets, Atmos. Chem. Phys., 18(15), 11247–11260,
- 1301 doi:10.5194/acp-18-11247-2018, 2018.
- 1302 Zheng, B., Tong, D., Li, M., Liu, F., Hong, C., Geng, G., Li, H., Li, X., Peng, L., Qi,
- 1303 J., Yan, L., Zhang, Y., Zhao, H., Zheng, Y., He, K. and Zhang, Q.: Trends in
- 1304 China's anthropogenic emissions since 2010 as the consequence of clean air
- 1305 actions, Atmos. Chem. Phys., doi:10.5194/acp-18-14095-2018, 2018.
- 1306 Zheng, Y., Che, H., Xia, X., Wang, Y., Wang, H., Wu, Y., Tao, J., Zhao, H., An, L.,
- 1307 Li, L., Gui, K., Sun, T., Li, X., Sheng, Z., Liu, C., Yang, X., Liang, Y., Zhang, L.,
- 1308 Liu, C., Kuang, X., Luo, S., You, Y. and Zhang, X.: Five-year observation of
- 1309 aerosol optical properties and its radiative effects to planetary boundary layer
- 1310 during air pollution episodes in North China: Intercomparison of a plain site and a
- 1311 mountainous site in Beijing, Sci. Total Environ.,
- 1312 doi:10.1016/J.SCITOTENV.2019.03.418, 2019.
- 1313



1314 **Table captions:**1315 **Table 1.** Prediction variables used in the stepwise MLR models.

1316

1317 **Figure captions:**

1318 **Figure 1.** Geographical locations of the AERONET (yellow dots) and CARSNET sites (magenta  
1319 dots) used in this work. The red boxes represent the 12 regions of interest selected in this study:  
1320 Northeast Asia (NEA), northern China (NC), southern China (SC), Southeast Asia (SEA),  
1321 Northwest China (NWC), South Asia (SA), Middle East (ME), western Europe (WEU), Sahara  
1322 Desert (SD), Central Africa (CF), eastern United States (EUS), and Amazon Zone (AMZ).

1323

1324 **Figure 2.** Validation of the combined AERONET and CARSNET AODs against the three-hourly  
1325 MERRA-2 AOD on the global scale. The color-coded dots indicate the number of samples. The  
1326 solid red line is the line of best fit and the black dashed line is the 1:1 line.

1327

1328 **Figure 3.** Comparison of the three-hourly MERRA-2 AOD datasets with AOD observations of  
1329 468 AERONET sites worldwide and 37 CARSNET sites in China: site performance maps for the  
1330 (a1) correlation coefficient ( $R$ ), (b1) mean absolute error (MAE) and root-mean-square error  
1331 (RMSE), and (c1) relative mean bias (RMB) between MERRA-2 AOD and ground-based  
1332 AERONET AOD observations. Panels (a2) to (c2) are enlarged site performance maps for  $R$ ,  
1333 MAE and RMSE, and RMB, respectively, using the CARSNET observations as reference. The  
1334 size of the circles in (b1) and (b2) represent the RMSE and their inner color represents the MAE.  
1335 Panels (a3), (b3), (b4) and (c3) are frequency distribution histograms for the  $R$ , RMSE, MAE and  
1336 RMB between MERRA-2 and all ground-based observations incorporating AERONET and  
1337 CARSNET, respectively. Note that all sites within each region of interest (ROI) are integrated to  
1338 assess the accuracy of the MERRA-2 AOD dataset in that area. The performance of the MERRA-2  
1339 AOD dataset in each ROI is illustrated in Figs. S2 and S3.

1340

1341 **Figure 4.** Temporal evolution of regional monthly averaged AOD for the 12 regions of interest.  
1342 Each year is represented by an irregular ring with 12 directions. Each direction of the ring  
1343 represents a specific month; the distance from the center of the ring represents the regional  
1344 monthly mean AOD value; and the color of the ring represents the year. A special ring colored  
1345 cyan represents the monthly mean AOD for the period 1980–2016.

1346

1347 **Figure 5.** Spatial distributions of the linear trends in annual and seasonal MERRA-2 AOD  
1348 calculated from the time series value of the de-seasonalized monthly anomaly during (a) 1980–  
1349 2016, (b) 1980–1997, and (c) 1998–2016. Only trend values with statistical significance at the 95%  
1350 confidence level are shown.

1351

1352 **Figure 6.** Spatial distributions of annual and seasonal trends in AOD calculated from the time  
1353 series value of the de-seasonalized monthly anomaly from (a) MERRA-2, (b) MODIS/Terra, and  
1354 MISR between 2001 and 2016. Only trend values with statistical significance at the 95%  
1355 confidence level are shown.



1356 **Figure 7.** Inter-comparisons of global and regional annual trends in AOD calculated from the time  
1357 series value of the de-seasonalized monthly anomaly of MERRA-2, MODIS/Terra and MISR,  
1358 during the four periods of 1980–2016, 1980–1997, 1998–2016, and 2001–2016. Error bars  
1359 represent the uncertainty associated with the calculated trend. The trend bars with shadow indicate  
1360 statistical significance at the 95% confidence level.

1361

1362 **Figure 8.** Sliding-window trend analyses of the annual mean MERRA-2 AOD from 1980 to 2016  
1363 over the 12 ROIs (see Fig. 1 for names and locations of regions), with at least 10 years used to  
1364 calculate trends. The *x*-axis and *y*-axis indicate the start year and the length of the time series to  
1365 calculate the trend, respectively. The colors of rectangles represent the intensity of the trend (units:  
1366 /year), and those with black ‘x’ signs indicate linear trends above the 95% significance level.

1367

1368 **Figure 9.** Temporal evolution of sliding decadal trends in the annual and seasonal mean AOD  
1369 from MERRA-2, MODIS/Terra and MISR over the 12 ROIs. The trends were calculated for each  
1370 10-year interval from 1980 to 2007 for MERRA-2, and from 2001 to 2007 for MODIS/Terra and  
1371 MISR. The colors of the rectangles represent the intensity of the decadal trend (units: /year), and  
1372 those with black ‘x’ signs indicate linear trends above the 95% significance level.

1373

1374 **Figure 10.** Spatial distributions of linear trends (units: kg/km<sup>2</sup>/year) in total anthropogenic  
1375 emissions of total suspended particles (TSP), SO<sub>2</sub>, black carbon (BC), and organic carbon (OC)  
1376 during 1980–2014 derived from the Peking University emissions inventory  
1377 (<http://inventory.pku.edu.cn/>) (Huang et al., 2014). Only linear trend values with statistical  
1378 significance at the 95% confidence level are shown.

1379

1380 **Figure 11.** Time series of MERRA-2 (in black) and modeled AOD monthly normalized anomalies  
1381 from 1980 to 2014 over the 12 regions of interest. The coefficient of determination ( $R^2$ ) of the  
1382 regression fit of the stepwise MLR model with emission factors (in blue), meteorology (in green),  
1383 and both emissions and meteorology (in red) as predictors are given in the top-right of each panel.

1384

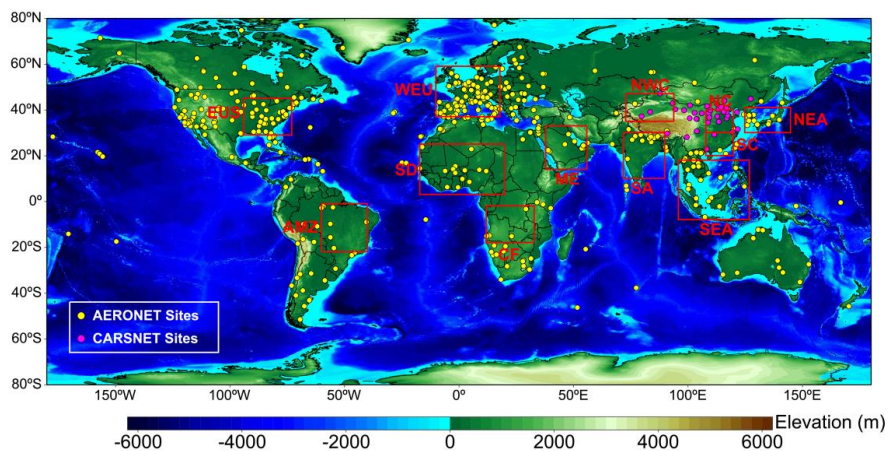
1385 **Figure 12.** The LMG method–estimated relative contributions (%) of total variances in the  
1386 stepwise MLR model explained by the local emission factors (left-hand bars) and meteorological  
1387 variables (right-hand bars) over the 12 regions of interest during three periods: (a) 1980–1997 (top  
1388 panel); (b) 1998–2014 (middle panel); and (c) 1980–2014 (bottom panel). Note that  
1389 meteorological parameters were combined as follows: temperature, T (Ts, T<sub>850</sub>, T<sub>700</sub>, T<sub>500</sub>, dT<sub>900-s</sub>,  
1390 dT<sub>850-s</sub>); geopotential height, GH (GH<sub>850</sub>, GH<sub>700</sub>, GH<sub>500</sub>); relative humidity, RH (RH<sub>s</sub>, RH<sub>850</sub>, RH<sub>700</sub>,  
1391 RH<sub>500</sub>); vertical velocity, Ome (Ome<sub>850</sub>, Ome<sub>700</sub>, Ome<sub>500</sub>); and wind speed, WS (U<sub>850</sub>, U<sub>700</sub>, U<sub>500</sub>,  
1392 V<sub>850</sub>, V<sub>700</sub>, V<sub>500</sub>, WS<sub>s</sub>, WS<sub>850</sub>, WS<sub>700</sub>, WS<sub>500</sub>, VWS<sub>500-850</sub>). Refer to Table S3 for the detailed  
1393 relative contributions of each variable in the stepwise MLR models.



1394 Table 1. Prediction variables used in the stepwise MLR models.

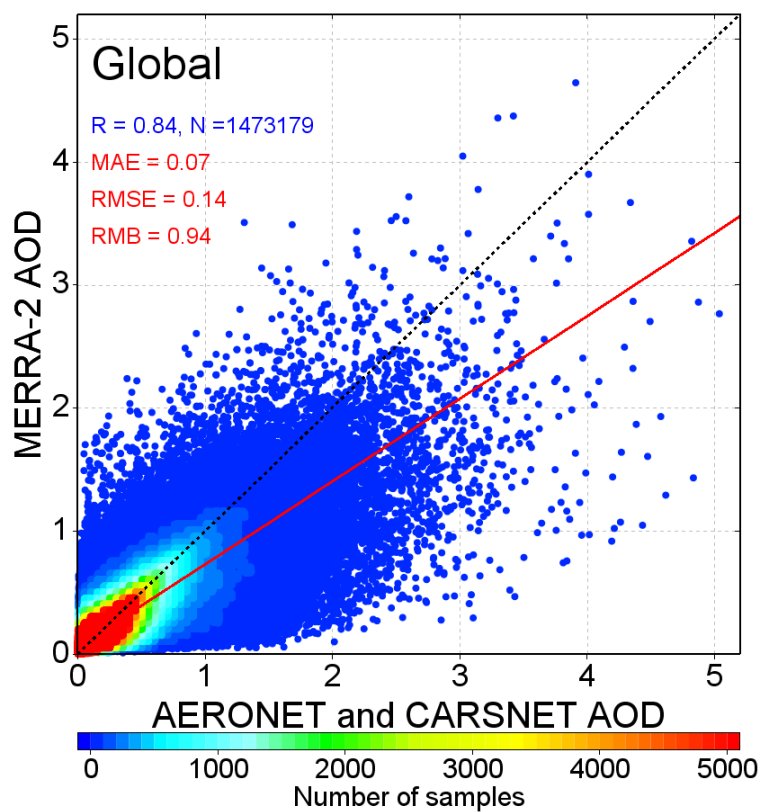
Data type	Variables	Predictors used in the stepwise MLR model <sup>a</sup>	Data source
Emission factors	TSP	Gridded monthly total emissions of total suspended particles	Peking University global emissions inventories at 1° × 1° horizontal resolution ( <a href="http://inventory.pku.edu.cn/home.html">http://inventory.pku.edu.cn/home.html</a> )
	SO <sub>2</sub>	Gridded monthly total emissions of sulfur dioxide	
	BC	Gridded monthly total emissions of black carbon	
	OC	Gridded monthly total emissions of organic carbon	
Meteorological parameters	Pre	Gridded monthly total surface precipitation	MERRA-2 reanalysis dataset at 0.5° × 0.625° horizontal resolution ( <a href="https://disc.gsfc.nasa.gov/daac-bin/FTPSubset2.pl">https://disc.gsfc.nasa.gov/daac-bin/FTPSubset2.pl</a> )
	PBLH	Gridded monthly mean planetary boundary layer height	
	SM	Gridded monthly mean soil moisture at surface	
	SLP	Gridded monthly mean sea level pressure	
	CLF	Gridded monthly mean cloud fraction	
	T <sub>s</sub>	Gridded monthly mean surface temperature	
	T	Gridded monthly mean 850-, 700- and 500-hPa temperature	
	dT	Gridded monthly mean temperature difference between 900 hPa and the surface, and 850 hPa and the surface	
	GH	Gridded monthly mean 850-, 700- and 500-hPa geopotential height	
	RH <sub>s</sub>	Gridded monthly mean surface relative humidity	
	RH	Gridded monthly mean 850-, 700- and 500-hPa relative humidity	
	Ome	Gridded monthly mean 850-, 700- and 500-hPa vertical velocity	
	U	Gridded monthly mean 850-, 700- and 500-hPa zonal wind	
V	Gridded monthly mean 850-, 700- and 500-hPa meridional wind		
WS <sub>s</sub>	Gridded monthly mean surface wind speed		
WS	Gridded monthly mean 850-, 700- and 500-hPa wind speed		
VS <sub>500-850</sub> <sup>b</sup>	Gridded monthly mean vertical wind shear between 500 and 850 hPa		

1395 <sup>a</sup>Units: g/km<sup>2</sup> (TSP, SO<sub>2</sub>, BC, OC); kg/m<sup>2</sup>/s (Pre); m (PBLH, GH); 1 (SM, CLF); Pa (SLP); K (T, dT); % (RH); pa/s (Ome); and m/s (U, V, WS, VWS<sub>500-850</sub>)1396 <sup>b</sup>VWS<sub>500-850</sub> was calculated as  $\sqrt{(U_{500} - U_{850})^2 + (V_{500} - V_{850})^2}$



1397  
1398  
1399  
1400  
1401  
1402  
1403  
1404

**Figure 1.** Geographical locations of the AERONET (yellow dots) and CARSNET sites (magenta dots) used in this work. The red boxes represent the 12 regions of interest selected in this study: Northeast Asia (NEA), northern China (NC), southern China (SC), Southeast Asia (SEA), Northwest China (NWC), South Asia (SA), Middle East (ME), western Europe (WEU), Sahara Desert (SD), Central Africa (CF), eastern United States (EUS), and Amazon Zone (AMZ).



1405

1406

**Figure 2.** Validation of the combined AERONET and CARSNET AODs against the three-hourly MERRA-2 AOD

1407

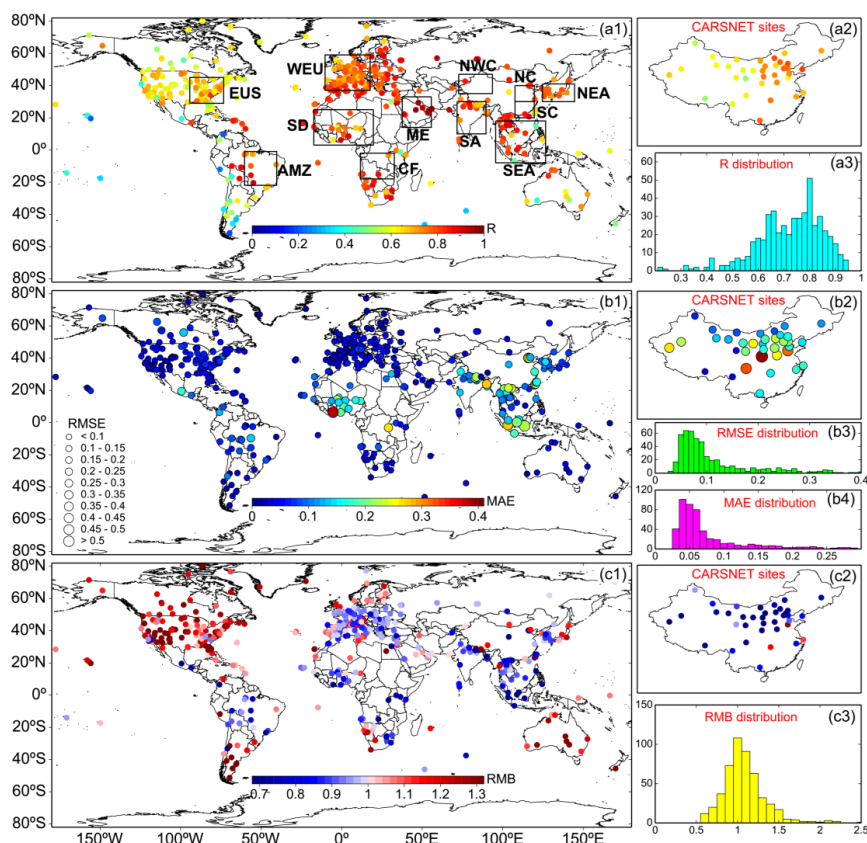
on the global scale. The color-coded dots indicate the number of samples. The solid red line is the line of best fit

1408

and the black dashed line is the 1:1 line.

1409

1410



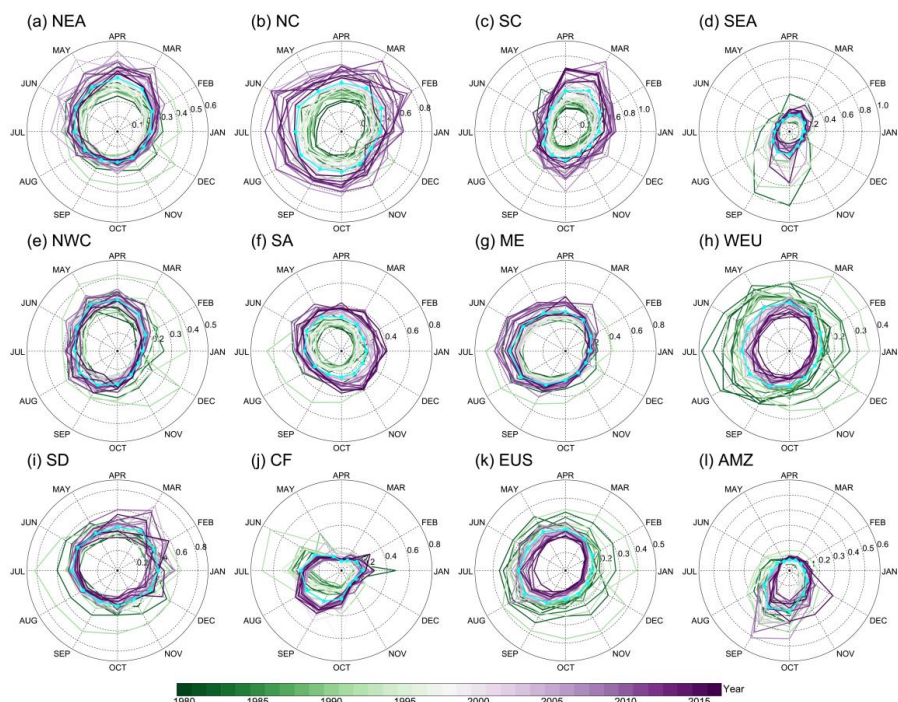
1411

1412 **Figure 3.** Comparison of the three-hourly MERRA-2 AOD datasets with AOD observations of 468 AERONET  
 1413 sites worldwide and 37 CARSNET sites in China: site performance maps for the (a1) correlation coefficient ( $R$ ),  
 1414 (b1) mean absolute error (MAE) and root-mean-square error (RMSE), and (c1) relative mean bias (RMB) between  
 1415 MERRA-2 AOD and ground-based AERONET AOD observations. Panels (a2) to (c2) are enlarged site  
 1416 performance maps for  $R$ , MAE and RMSE, and RMB, respectively, using the CARSNET observations as reference.  
 1417 The size of the circles in (b1) and (b2) represent the RMSE and their inner color represents the MAE. Panels (a3),  
 1418 (b3), (b4) and (c3) are frequency distribution histograms for the  $R$ , RMSE, MAE and RMB between MERRA-2  
 1419 and all ground-based observations incorporating AERONET and CARSNET, respectively. Note that all sites within  
 1420 each region of interest (ROI) are integrated to assess the accuracy of the MERRA-2 AOD dataset in that area. The  
 1421 performance of the MERRA-2 AOD dataset in each ROI is illustrated in Figs. S2 and S3.

1422

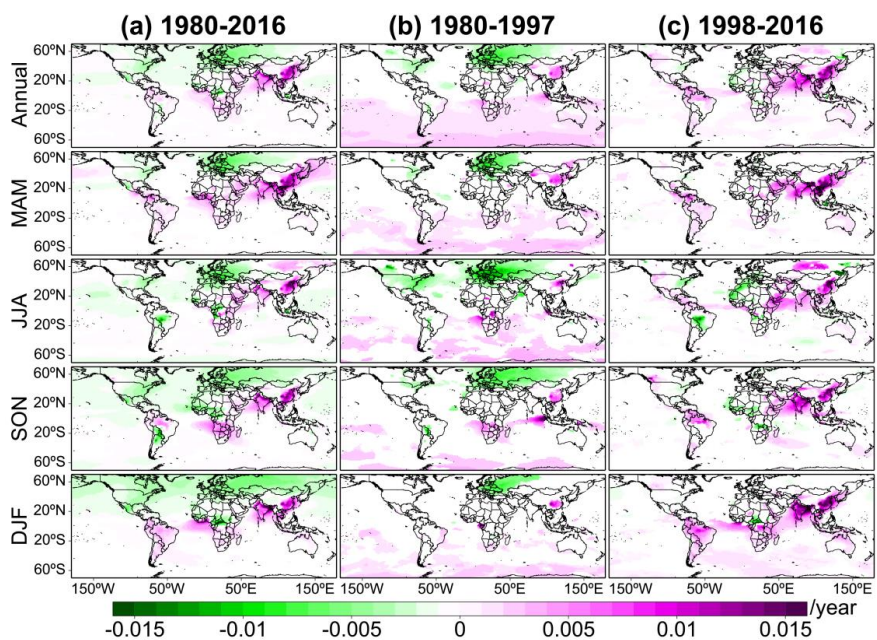
1423





1424  
1425  
1426  
1427  
1428  
1429  
1430

**Figure 4.** Temporal evolution of regional monthly averaged AOD for the 12 regions of interest. Each year is represented by an irregular ring with 12 directions. Each direction of the ring represents a specific month; the distance from the center of the ring represents the regional monthly mean AOD value; and the color of the ring represents the year. A special ring colored cyan represents the monthly mean AOD for the period 1980–2016.



1431

1432

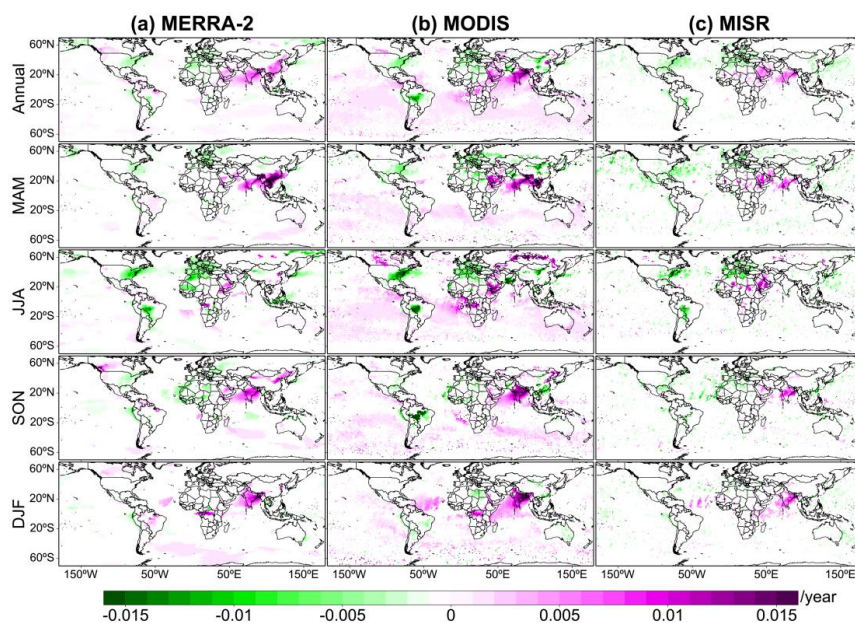
1433

1434

1435

1436

**Figure 5.** Spatial distributions of the linear trends in annual and seasonal MERRA-2 AOD calculated from the time series value of the de-seasonalized monthly anomaly during (a) 1980–2016, (b) 1980–1997, and (c) 1998–2016. Only trend values with statistical significance at the 95% confidence level are shown.



1437

1438

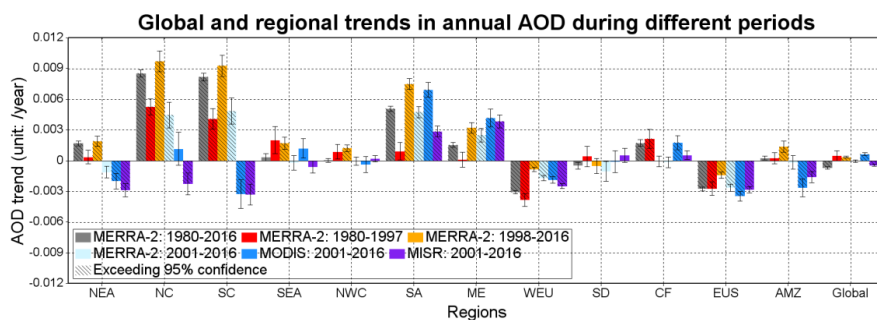
1439

1440

1441

1442

**Figure 6.** Spatial distributions of annual and seasonal trends in AOD calculated from the time series value of the de-seasonalized monthly anomaly from (a) MERRA-2, (b) MODIS/Terra, and (c) MISR between 2001 and 2016. Only trend values with statistical significance at the 95% confidence level are shown.

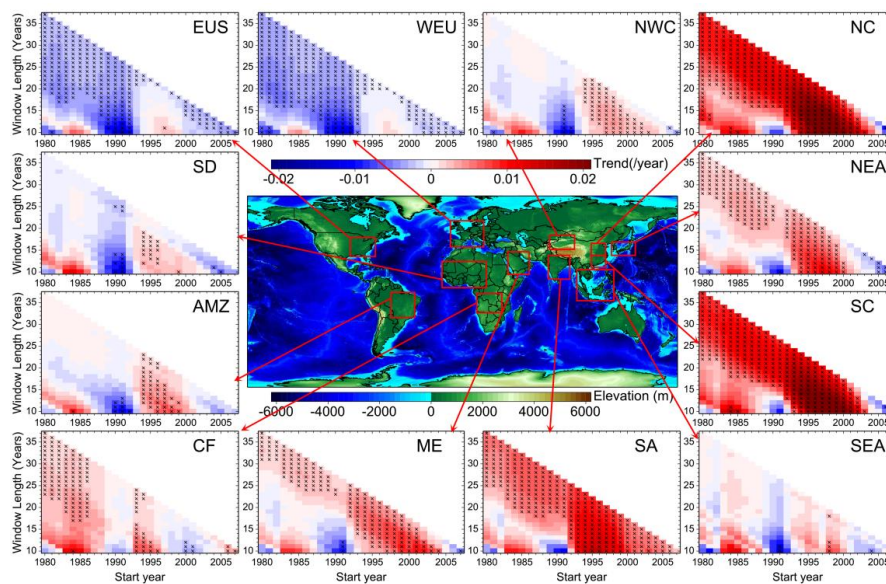


1443

1444 **Figure 7.** Inter-comparisons of global and regional annual trends in AOD calculated from the time series value of  
1445 the de-seasonalized monthly anomaly of MERRA-2, MODIS/Terra and MISR, during the four periods of 1980–  
1446 2016, 1980–1997, 1998–2016, and 2001–2016. Error bars represent the uncertainty associated with the calculated  
1447 trend. The trend bars with shadow indicate statistical significance at the 95% confidence level.

1448

1449



1450

1451

1452

1453

1454

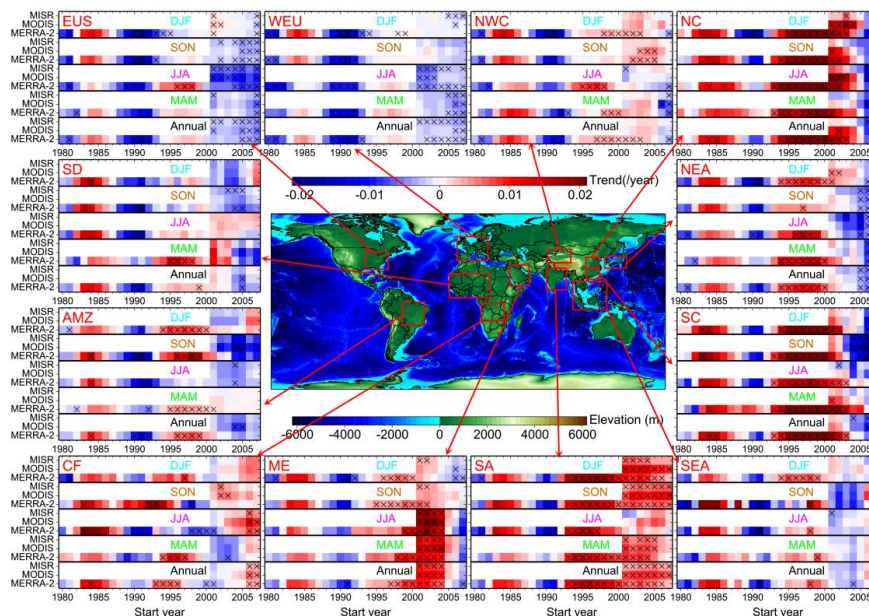
1455

1456

1457

**Figure 8.** Sliding-window trend analyses of the annual mean MERRA-2 AOD from 1980 to 2016 over the 12 ROIs (see Fig. 1 for names and locations of regions), with at least 10 years used to calculate trends. The *x*-axis and *y*-axis indicate the start year and the length of the time series to calculate the trend, respectively. The colors of rectangles represent the intensity of the trend (units: /year), and those with black 'x' signs indicate linear trends above the 95% significance level.

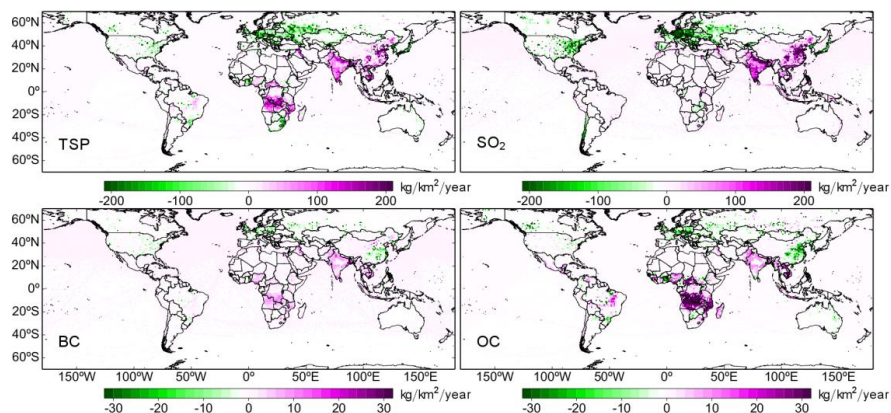




1458  
1459  
1460  
1461  
1462  
1463  
1464  
1465

**Figure 9.** Temporal evolution of sliding decadal trends in the annual and seasonal mean AOD from MERRA-2, MODIS/Terra and MISR over the 12 ROIs. The trends were calculated for each 10-year interval from 1980 to 2007 for MERRA-2, and from 2001 to 2007 for MODIS/Terra and MISR. The colors of the rectangles represent the intensity of the decadal trend (units: /year), and those with black 'x' signs indicate linear trends above the 95% significance level.



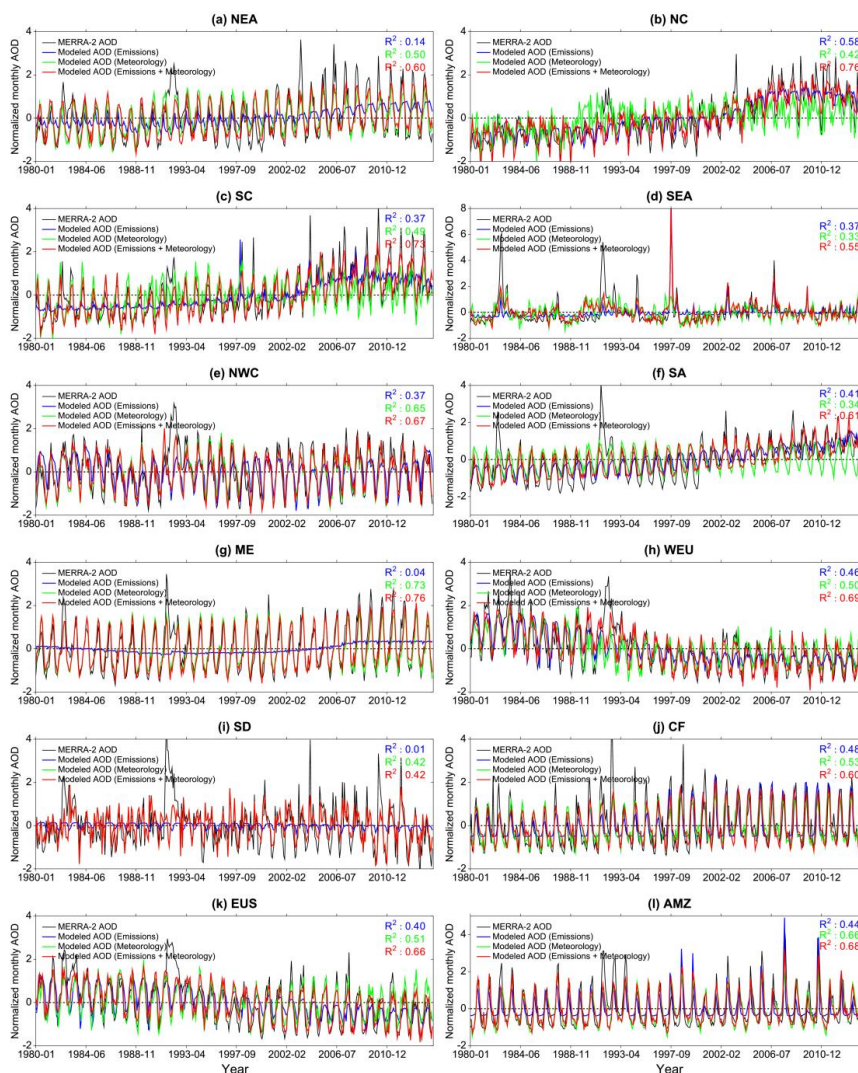


1466

1467 **Figure 10.** Spatial distributions of linear trends (units:  $\text{kg}/\text{km}^2/\text{year}$ ) in total anthropogenic emissions of total  
1468 suspended particles (TSP),  $\text{SO}_2$ , black carbon (BC), and organic carbon (OC) during 1980–2014 derived from the  
1469 Peking University emissions inventory (<http://inventory.pku.edu.cn/>) (Huang et al., 2014). Only linear trend values  
1470 with statistical significance at the 95% confidence level are shown.

1471

1472



1473

1474

1475

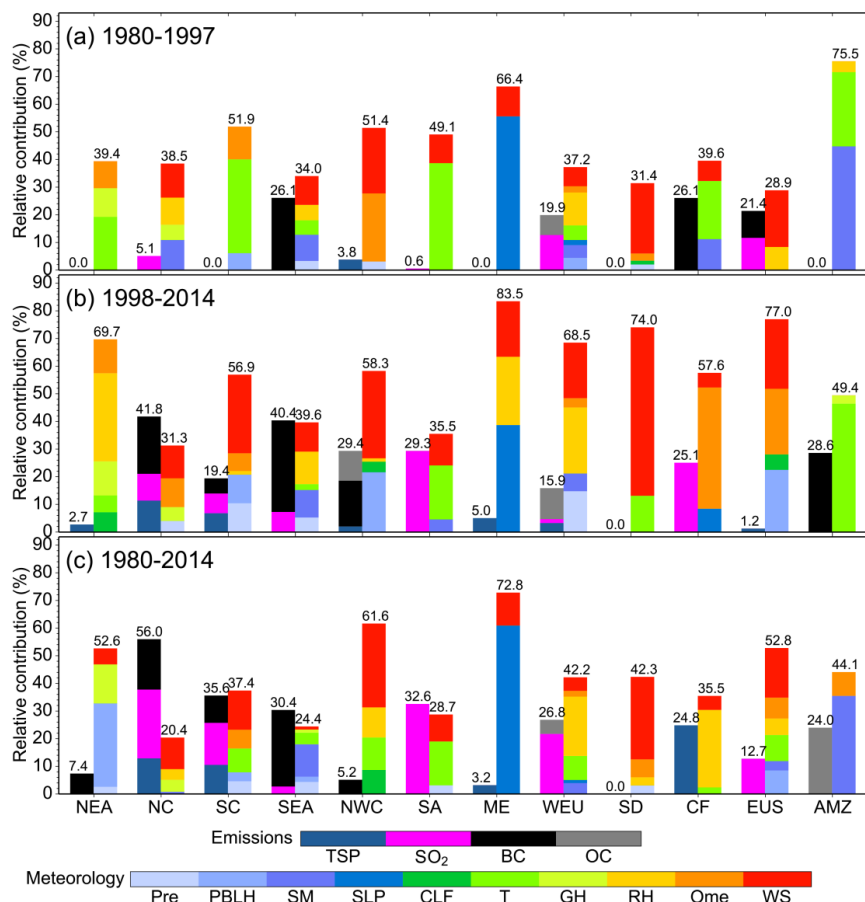
1476

1477

1478

1479

**Figure 11.** Time series of MERRA-2 (in black) and modeled AOD monthly normalized anomalies from 1980 to 2014 over the 12 regions of interest. The coefficient of determination ( $R^2$ ) of the regression fit of the stepwise MLR model with emission factors (in blue), meteorology (in green), and both emissions and meteorology (in red) as predictors are given in the top-right of each panel.



1480  
 1481  
 1482  
 1483  
 1484  
 1485  
 1486  
 1487  
 1488  
 1489

**Figure 12.** The LMG method–estimated relative contributions (%) of total variances in the stepwise MLR model explained by the local emission factors (left-hand bars) and meteorological variables (right-hand bars) over the 12 regions of interest during three periods: (a) 1980–1997 (top panel); (b) 1998–2014 (middle panel); and (c) 1980–2014 (bottom panel). Note that meteorological parameters were combined as follows: temperature, T (Ts, T<sub>850</sub>, T<sub>700</sub>, T<sub>500</sub>, dT<sub>900-850</sub>, dT<sub>850-500</sub>); geopotential height, GH (GH<sub>850</sub>, GH<sub>700</sub>, GH<sub>500</sub>); relative humidity, RH (RH<sub>s</sub>, RH<sub>850</sub>, RH<sub>700</sub>, RH<sub>500</sub>); vertical velocity, Ome (Ome<sub>850</sub>, Ome<sub>700</sub>, Ome<sub>500</sub>); and wind speed, WS (U<sub>850</sub>, U<sub>700</sub>, U<sub>500</sub>, V<sub>850</sub>, V<sub>700</sub>, V<sub>500</sub>, WS<sub>s</sub>, WS<sub>850</sub>, WS<sub>700</sub>, WS<sub>500</sub>, VWS<sub>500-850</sub>). Refer to Table S3 for the detailed relative contributions of each variable in the stepwise MLR models.